Penalty coupling of non-matching isogeometric Kirchhoff–Love shell patches with application to composite wind turbine blades

Austin J. Herrema[a,1], Emily L. Johnson[a,1], Davide Proserpio[b,1], Michael C.H. Wu[a], Josef Kiendl[b], Ming-Chen Hsu[a,*]

[a]*Department of Mechanical Engineering, Iowa State University, 2025 Black Engineering, Ames, IA 50011, USA*
[b]*Department of Marine Technology, Norwegian University of Science and Technology, O. Nielsens veg 10, 7052 Trondheim, Norway*

Abstract

Isogeometric analysis (IGA) has been a particularly impactful development in the realm of Kirchhoff–Love thin-shell analysis because the high-order basis functions employed naturally satisfy the requirement of C^1 continuity. Still, engineering models of appreciable complexity, such as wind turbine blades, are typically modeled using multiple surface patches and, often, neither rotational continuity nor conforming discretization can be practically obtained at patch interfaces. A penalty approach for coupling adjacent patches is therefore presented. The proposed method imposes both displacement and rotational continuity and is applicable to either smooth or non-smooth interfaces and either matching or non-matching discretization. The penalty formulations require only a single, dimensionless penalty coefficient for both displacement and rotation coupling terms, alleviating the problem-dependent nature of the penalty parameters. Using this coupling methodology, numerous benchmark problems encapsulating a variety of analysis types, geometrical and material properties, and matching and non-matching interfaces are addressed. The coupling methodology produces consistently accurate results throughout all tests. Furthermore, the suggested penalty coefficient of $\alpha = 10^3$ is shown to be effective for the wide range of problem configurations addressed. Finally, a realistic wind turbine blade model, consisting of 27 patches and 51 coupling interfaces and having a chordwise- and spanwise-variant composite material definition, is subjected to buckling, vibration, and nonlinear deformation analyses using the proposed approach.

Keywords: isogeometric analysis; Kirchhoff–Love shell; patch coupling; penalty parameter; non-matching interface; wind turbine blade

*Corresponding author
Email addresses: josef.kiendl@ntnu.no (Josef Kiendl), jmchsu@iastate.edu (Ming-Chen Hsu)
[1]These three authors contributed equally to this work.

The final publication is available at Elsevier via https://doi.org/10.1016/j.cma.2018.08.038

Contents

1. Introduction

Modern engineering industries often commit significant resources to performing numerical analyses based on the finite element method. Yet, significant portions of the design-and-analysis workflow are consumed by time-consuming and labor-intensive activities such as model cleanup and finite element mesh generation [1]. Hughes et al. [2] sought to improve this outlook with the introduction of isogeometric analysis (IGA), an analysis approach in which the functions employed by computer-aided design (CAD) software are directly employed as finite element bases during analysis. Isogeometric analysis has been particularly impactful in the realm of thin-shell analysis [3–7]. Kirchhoff–Love theory is typically applied to thin-shell structures—indicated by $R/t \geq 20$, where R is the shell's radius of curvature and t is its thickness [8]—and assumes that

transverse shear strains are negligible, a reasonable assumption for many shell structures of interest. Importantly, second-order derivatives appear in the governing variational equations of the Kirchhoff–Love theory; this implies the necessity of C^1-continuous approximation functions. This condition has always been a major obstacle for the development of efficient finite element thin-shell formulations. However, in isogeometric Kirchhoff–Love shell analysis that uses, for example, non-uniform rational B-splines (NURBS), the most widely used spline-based mathematical functions in CAD and IGA, the C^1-smoothness requirement can be naturally satisfied in the interior of NURBS patches.

Models of complex, real-world objects, such as wind turbine blades, tend to be composed of multiple patches due to practical or technical limitations in geometry modeling or to capture design features such as material discontinuities. Despite the many potential advantages offered by isogeometric Kirchhoff–Love shells, they cannot be readily applied to such complex, multi-patch designs; additional action must be taken to enforce continuity at patch interfaces. Firstly, the patches must be connected, i.e., C^0 continuity must be imposed. For conforming meshes, where the control points of the two patches are co-located at their interface, this can be easily done by directly coupling the degrees of freedom of the boundary control points on both patches. This is not possible, however, in the case of non-conforming patches (patches which do share a common boundary in the physical space but have different discretizations along that boundary), or when patches only approximately share a common boundary in the physical space, a possible result of CAD modeling operations. The term *non-matching* is used to refer to both of these situations. In traditional finite element analysis, such geometric mismatches are typically corrected during mesh generation, ensuring that the resultant mesh is analysis-suitable. Because IGA circumvents mesh generation procedures, however, the analysis method itself must be capable of coupling non-matching patches. Additionally, for Kirchhoff–Love shell analysis, C^1 continuity must also be imposed on patch boundaries. Strictly speaking, C^1 continuity applies only to smooth patch interfaces, while complex shell structures typically also include non-smooth patch interfaces, i.e., patches joined with an angle other than 180 degrees. In such cases, it is the angle between the patches that must be maintained during deformation analysis. Therefore, the term *rotational continuity*, rather than C^1 continuity, is used when referring to patch interfaces of arbitrary angle (including smooth interfaces). Accordingly, C^0 continuity is referred to as *displacement continuity*.

A significant amount of research effort has been devoted to imposing rotational continuity within isogeometric Kirchhoff–Love shell analysis of multi-patch structures. In Kiendl et al. [3], it was shown that, for smooth and conforming patches, the constraint can be fulfilled by direct coupling of degrees of freedom of the first two rows of control points along the joint boundary, provided that the control points across this common edge are collinear. As a more general alternative, the bending strip method was introduced by Kiendl et al. [9]. It is a penalty-like approach,

which can couple both smooth and non-smooth patch interfaces. Goyal and Simeon [10] extended the bending strip approach by proposing alternate formulations that improve problem conditioning. In all cases, however, the bending strip method is still restricted to conforming discretizations. Lei et al. [11], instead, presented a penalty formulation that can handle non-conforming meshes. However, the method is restricted to smooth patch interfaces. Breitenberger et al. [12] have used penalty formulations for both displacement and rotational continuity and applied them to complex B-rep CAD models with non-matching interfaces. However, their formulation for rotational continuity was restricted to rotational deformation less than 90°, which is a significant limitation in large deformation analysis and for rotating structures. Duong et al. [13] proposed a different penalty formulation for rotational continuity, which has no restrictions on the rotational deformation. However, it was limited to conforming patch interfaces and the penalty parameters must be selected in a problem-dependent fashion.

Mortar methods have also been used for patch coupling in the context of IGA [14, 15]. However, the mortar method requires solving a saddle point problem for the Lagrange multiplier which can sometimes be challenging. Guo et al. [16, 17] and Nguyen-Thanh et al. [18] have developed formulations for Kirchhoff–Love shell patch coupling based on Nitsche's method. The advantage of such formulations is that they are less dependent on stabilization or penalty parameters than penalty methods. However, the formulations depend on the variational formulation employed and, as a result, are relatively difficult to implement for general-purpose analysis codes. Citing the complexity of Nitsche's method, Coox et al. [19] alternatively proposed a Virtual Uncommon-Knot-Inserted Master–Slave (VUKIMS) coupling technique based on master–slave interface constraints derived from the interface knot vectors.

The general advantage of penalty methods lies in their simplicity and flexibility. However, an inherent issue in these methods is the choice of penalty parameters. If the value of the penalty parameter is too low, the constraint is not satisfied accurately enough. If the penalty parameter value is too high, the matrices may become ill-conditioned and the solution of the linear system is prone to large numerical errors. Ideally, penalty formulations should scale with geometric and material properties in a way that makes the choice of the penalty parameters problem-independent. Otherwise, these parameters have to be chosen ad-hoc for each problem. They also should scale with the element size in order to make sure that the penalty error decreases with mesh refinement. When different constraints, like displacement and rotational continuity, are to be imposed simultaneously with penalty formulations, one also has to ensure the correct balance between the different penalty parameters. This can be very challenging when these parameters are chosen ad-hoc.

In this paper, we present novel penalty formulations for imposing both displacement and rotational continuity in multi-patch Kirchhoff–Love shell analysis. The proposed formulations work for smooth and non-smooth, matching and non-matching (or conforming and non-conforming)

patch interfaces. Both displacement and rotational continuity are controlled by a single, dimensionless penalty coefficient and proper scaling of the different penalty terms with the geometric and material parameters of the problem allows for a problem-independent choice of the penalty coefficient value. The presented approach shares similarities with those in Breitenberger et al. [12] and Duong et al. [13]. However, it is shown that the choice of the penalty parameter values is heavily problem-dependent in those formulations. The presented formulation is tested on a large series of benchmark problems, from linear to nonlinear analysis and from isotropic to composite materials. The examples demonstrate the accuracy and robustness of the proposed method. As a result of these studies, a universal recommendation for the choice of the penalty coefficient is obtained.

This paper is outlined as follows. In Section 2, the isogeometric Kirchhoff–Love shell formulation and the penalty formulation for patch coupling are presented. An effective selection of penalty parameters is also proposed. In Section 3, the formulations are evaluated using several linear and nonlinear benchmark problems, and the effective range of the relatively problem-agnostic penalty coefficient is demonstrated. In Section 4, the proposed method is applied to the structural analysis of a realistic composite wind turbine blade; the effectiveness of the method is demonstrated using linear buckling, vibration, and nonlinear deflection analyses. In Section 5, conclusions are drawn.

2. Shell formulations

2.1. Composite isogeometric Kirchhoff–Love shells

The proposed penalty formulation is dependent on the Kirchhoff–Love shell formulation itself. Thus, a brief review of the shell formulation is provided. An isogeometric Kirchhoff–Love thin-shell formulation was first proposed by Kiendl et al. [3] and was reformulated for composite shells in Bazilevs et al. [20]. The shell formulation is extended to handle general hyperelastic materials in Kiendl et al. [6]. The details relevant to the penalty formulation for patch coupling are given here. The variational formulation is based on the principle of virtual work:

$$\delta W = \delta W^{\text{int}} - \delta W^{\text{ext}} = 0 \,, \tag{1}$$

where W is the total work, W^{int} is the internal work, W^{ext} is the external work, and δ denotes a variation with respect to the virtual displacement variables $\delta\mathbf{u}$:

$$\delta W = \frac{\partial W}{\partial \mathbf{u}} \delta\mathbf{u} \,. \tag{2}$$

The internal virtual work is given by

$$\delta W^{\text{int}} = \int_{\Omega} (\mathbf{S} : \delta\mathbf{E}) \, \mathrm{d}\Omega \, , \tag{3}$$

where Ω is the shell volume in the undeformed configuration, $\mathbf{S}$ is the second Piola–Kirchhoff stress tensor, and $\mathbf{E}$ is the Green–Lagrange strain tensor.

For the Kirchhoff–Love shell theory, both normal and transverse shear strains are neglected; only the in-plane strain components are considered. The Green–Lagrange strain is assumed to vary linearly through the shell thickness and can be expressed as a combination of membrane and bending strains of the midsurface. Let Greek indices $\alpha = 1, 2$ and $\beta = 1, 2$ denote the in-plane components. The covariant components of $\mathbf{E}$ can be obtained as

$$E_{\alpha\beta} = \varepsilon_{\alpha\beta} + \xi_3 \kappa_{\alpha\beta} \, , \tag{4}$$

where $\varepsilon_{\alpha\beta}$ and $\kappa_{\alpha\beta}$ are the covariant components of the membrane strain tensor, $\boldsymbol{\varepsilon}$, and curvature change (due to bending) tensor, $\boldsymbol{\kappa}$, of the midsurface, respectively, $\xi_3 \in [-0.5t, 0.5t]$ is the through-thickness coordinate, and t is the thickness of the shell. Let $\mathbf{r}(\xi_1, \xi_2)$ be the spatial coordinate of the midsurface in the deformed configuration with ξ_1 and ξ_2 being the parametric coordinates used in defining the midsurface, and $\mathbf{a}_\alpha$ be the covariant surface basis vectors in the deformed configurations, obtained as $\mathbf{a}_\alpha = \mathbf{r}_{,\alpha}$, where $(\cdot)_{,\alpha} = \partial(\cdot)/\partial\xi_\alpha$ indicates the partial derivatives with respect to ξ_α. Let geometric variables indicated by $\mathring{(\cdot)}$ refer to the undeformed configuration. Membrane strain and curvature change coefficients are defined as

$$\varepsilon_{\alpha\beta} = \frac{1}{2}\left(\mathbf{a}_\alpha \cdot \mathbf{a}_\beta - \mathring{\mathbf{a}}_\alpha \cdot \mathring{\mathbf{a}}_\beta\right) \, , \tag{5}$$

$$\kappa_{\alpha\beta} = \mathring{\mathbf{a}}_{\alpha,\beta} \cdot \mathring{\mathbf{a}}_3 - \mathbf{a}_{\alpha,\beta} \cdot \mathbf{a}_3 \, , \tag{6}$$

where $\mathbf{a}_3$ is the unit vector normal to the shell midsurface in the deformed configuration, given by

$$\mathbf{a}_3 = \frac{\mathbf{a}_1 \times \mathbf{a}_2}{\|\mathbf{a}_1 \times \mathbf{a}_2\|} \, . \tag{7}$$

In this work, linear elastic material behavior is assumed, corresponding to a St. Venant–Kirchhoff material model. The stress–strain relationship is expressed by

$$\mathbf{S} = \mathbb{C}\mathbf{E} \, , \tag{8}$$

where $\mathbb{C}$ is a constitutive material tensor. Introducing Eq. (8) into Eq. (3), separating out the through-thickness integration, and utilizing the definition of the strain tensor $\mathbf{E}$ given in Eq. (4),

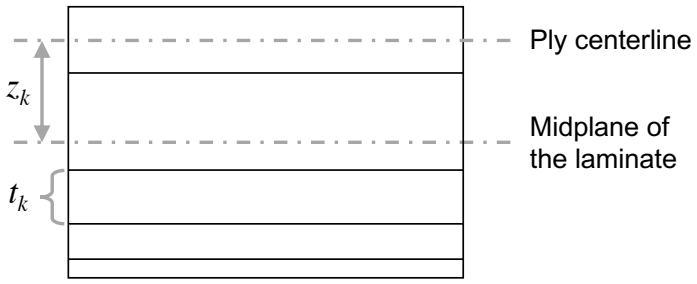

Figure 1: Composite layup with non-uniform and non-symmetric ply distribution.

one obtains

$$\delta W^{\text{int}} = \int_{\mathcal{S}} \delta\boldsymbol{\varepsilon} : \left(\left(\int_{-t/2}^{t/2} \mathbb{C} \, \mathrm{d}\xi_3 \right) \boldsymbol{\varepsilon} + \left(\int_{-t/2}^{t/2} \xi_3 \mathbb{C} \, \mathrm{d}\xi_3 \right) \boldsymbol{\kappa} \right) \mathrm{d}\mathcal{S} + \int_{\mathcal{S}} \delta\boldsymbol{\kappa} : \left(\left(\int_{-t/2}^{t/2} \xi_3 \mathbb{C} \, \mathrm{d}\xi_3 \right) \boldsymbol{\varepsilon} + \left(\int_{-t/2}^{t/2} \xi_3^2 \mathbb{C} \, \mathrm{d}\xi_3 \right) \boldsymbol{\kappa} \right) \mathrm{d}\mathcal{S} \,, \tag{9}$$

where $\mathcal{S}$ is the shell surface domain. In the case of composite materials, the structure is assumed to be composed of a number of orthotropic plies. Let k be the index of each ply and $\mathbb{C}_k$ be the material tensor of each ply obtained by transforming its orthotropic material tensor from the ply material coordinates to the shell coordinates. According to the classical laminate theory [21], the homogenized extensional (membrane) stiffness, $\mathbb{A}$, coupling stiffness, $\mathbb{B}$, and bending stiffness, $\mathbb{D}$, are given by

$$\mathbb{A} = \int_{-t/2}^{t/2} \mathbb{C} \, \mathrm{d}\xi_3 = \sum_{k=1}^{n} \mathbb{C}_k t_k \,, \tag{10}$$

$$\mathbb{B} = \int_{-t/2}^{t/2} \xi_3 \mathbb{C} \, \mathrm{d}\xi_3 = \sum_{k=1}^{n} \mathbb{C}_k t_k z_k \,, \tag{11}$$

$$\mathbb{D} = \int_{-t/2}^{t/2} \xi_3^2 \mathbb{C} \, \mathrm{d}\xi_3 = \sum_{k=1}^{n} \mathbb{C}_k \left(t_k z_k^2 + \frac{t_k^3}{12} \right) . \tag{12}$$

In the above, n is the total number of piles, t_k is the thickness of the kth ply, and z_k is the distance from the centroid of the kth ply to the mid-plane of the laminate, as illustrated in Figure 1. The internal virtual work for a composite shell can therefore be defined:

$$\delta W^{\text{int}} = \int_{\mathcal{S}} \delta\boldsymbol{\varepsilon} : (\mathbb{A}\boldsymbol{\varepsilon} + \mathbb{B}\boldsymbol{\kappa}) \, \mathrm{d}\mathcal{S} + \int_{\mathcal{S}} \delta\boldsymbol{\kappa} : (\mathbb{B}\boldsymbol{\varepsilon} + \mathbb{D}\boldsymbol{\kappa}) \, \mathrm{d}\mathcal{S} \,. \tag{13}$$

More details about this formulation can be found in Kiendl [22].

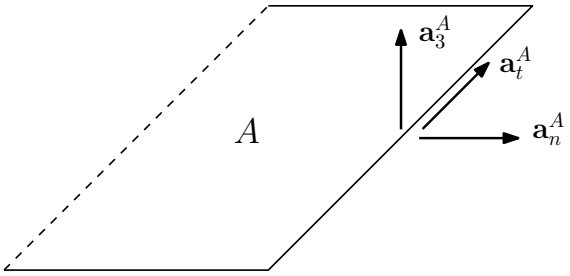

Figure 2: The unit normal vector, $\mathbf{a}_3^{\mathrm{A}}$; unit tangent vector, $\mathbf{a}_t^{\mathrm{A}}$; and in-plane unit normal vector, $\mathbf{a}_n^{\mathrm{A}}$, at an edge of patch $\mathcal{S}^{\mathrm{A}}$.

2.2. A penalty formulation for non-matching patch coupling

A penalty approach for coupling adjacent patches having either matching or non-matching discretization and either smooth or non-smooth interfaces is presented here. In the following, it is assumed that there are two patches, $\mathcal{S}^{\mathrm{A}}$ and $\mathcal{S}^{\mathrm{B}}$, which, in the undeformed configuration, are approximately co-located along an interface curve, $\mathcal{L}$. For enforcing displacement continuity between the two patches, the following penalty virtual work is introduced:

$$\delta W^{\mathrm{pd}} = \int_{\mathcal{L}} \alpha_{\mathrm{d}} \left(\mathbf{u}^{\mathrm{A}} - \mathbf{u}^{\mathrm{B}}\right) \cdot \left(\delta\mathbf{u}^{\mathrm{A}} - \delta\mathbf{u}^{\mathrm{B}}\right) \mathrm{d}\mathcal{L} \,, \tag{14}$$

where superscripts A and B indicate quantities evaluated on patches $\mathcal{S}^{\mathrm{A}}$ or $\mathcal{S}^{\mathrm{B}}$, respectively, α_{d} is a penalty parameter of large magnitude, further discussed in the following section, and $\mathbf{u}^{\mathrm{A}}$ and $\mathbf{u}^{\mathrm{B}}$ are the displacements of corresponding locations on $\mathcal{S}^{\mathrm{A}}$ and $\mathcal{S}^{\mathrm{B}}$, respectively, along $\mathcal{L}$. Equation (14) dictates that, if the distance between points on $\mathcal{S}^{\mathrm{A}}$ and $\mathcal{S}^{\mathrm{B}}$ is not the same in the deformed and undeformed configurations, a large penalty energy is introduced into the system.

The coupling methodology must also maintain the angle formed by patches $\mathcal{S}^{\mathrm{A}}$ and $\mathcal{S}^{\mathrm{B}}$. For imposing rotational continuity between two patches, the following penalty virtual work is introduced:

$$\begin{aligned}\delta W^{\mathrm{pr}} = \int_{\mathcal{L}} \alpha_{\mathrm{r}} \Big(&\left(\mathbf{a}_3^{\mathrm{A}} \cdot \mathbf{a}_3^{\mathrm{B}} - \mathring{\mathbf{a}}_3^{\mathrm{A}} \cdot \mathring{\mathbf{a}}_3^{\mathrm{B}}\right)\left(\delta\mathbf{a}_3^{\mathrm{A}} \cdot \mathbf{a}_3^{\mathrm{B}} + \mathbf{a}_3^{\mathrm{A}} \cdot \delta\mathbf{a}_3^{\mathrm{B}}\right) \\ &+ \left(\mathbf{a}_n^{\mathrm{A}} \cdot \mathbf{a}_3^{\mathrm{B}} - \mathring{\mathbf{a}}_n^{\mathrm{A}} \cdot \mathring{\mathbf{a}}_3^{\mathrm{B}}\right)\left(\delta\mathbf{a}_n^{\mathrm{A}} \cdot \mathbf{a}_3^{\mathrm{B}} + \mathbf{a}_n^{\mathrm{A}} \cdot \delta\mathbf{a}_3^{\mathrm{B}}\right)\Big) \mathrm{d}\mathcal{L} \,,\end{aligned} \tag{15}$$

where α_{r} is a penalty parameter that will be discussed in detail in the following section. In Eq. (15), we introduce the in-plane unit normal vector, $\mathbf{a}_n^{\mathrm{A}}$, which lies in the plane of patch $\mathcal{S}^{\mathrm{A}}$ and is orthogonal to the penalty curve, $\mathcal{L}$. Given the natural tangent vector of the penalty curve on patch $\mathcal{S}^{\mathrm{A}}$, $\tilde{\mathbf{a}}_t^{\mathrm{A}}$, its unit vector, $\mathbf{a}_t^{\mathrm{A}}$, can be obtained as $\mathbf{a}_t^{\mathrm{A}} = \tilde{\mathbf{a}}_t^{\mathrm{A}} / \|\tilde{\mathbf{a}}_t^{\mathrm{A}}\|$. $\mathbf{a}_n^{\mathrm{A}}$ can then be computed as $\mathbf{a}_n^{\mathrm{A}} = \mathbf{a}_t^{\mathrm{A}} \times \mathbf{a}_3^{\mathrm{A}}$ (see Figure 2). Note that $\mathbf{a}_t^{\mathrm{A}}$ and $\mathbf{a}_3^{\mathrm{A}}$ are orthogonal unit vectors.

The first term on the right hand side of Eq. (15) penalizes variations in the scalar product of the

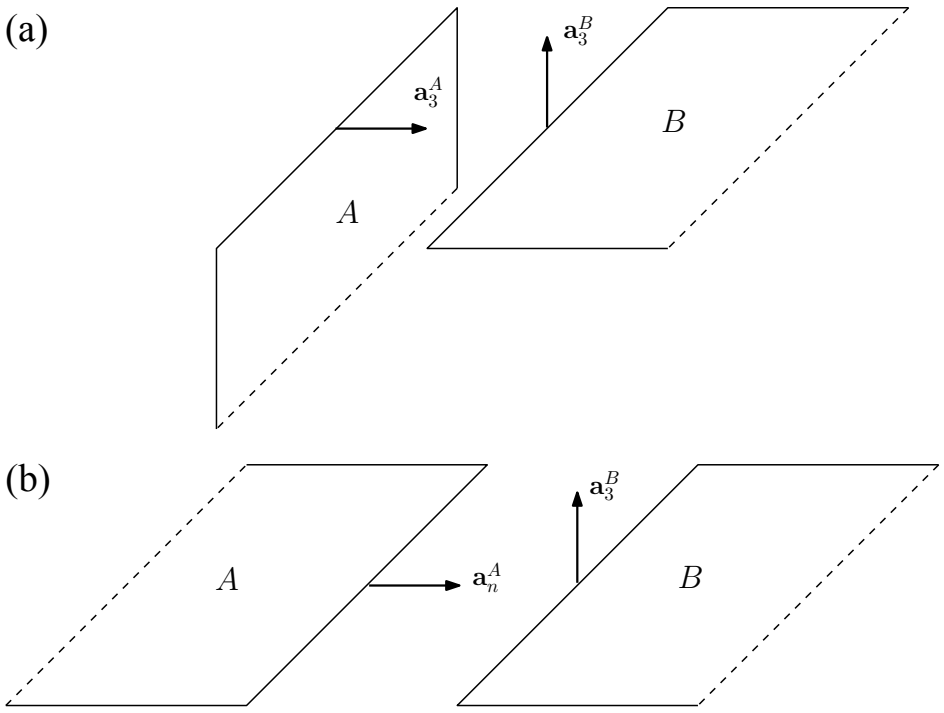

Figure 3: Patch interfaces having an interface angle of (a) 90 degrees and (b) 180 degrees.

normal vectors of the two patches. As will be shown in more detail later, the variation of the scalar product of two parallel unit vectors vanishes; thus, the formulation is enhanced by the second term which penalizes variations in the scalar product of the in-plane normal vector of patch $\mathcal{S}^{\mathrm{A}}$ and the normal vector of patch $\mathcal{S}^{\mathrm{B}}$. Regardless of the patch angle, both terms are calculated and added together. With this combination, the patches are allowed to form arbitrary angles at their interface. For patch interfaces forming an angle of 90°, see Figure 3a, only the first term is active. For patches having an angle of 180° at their interface, see Figure 3b, only the second term is active. For all other interface angles, both terms are active with complementary strengths.

Finally, the virtual work formulation, Eq. (1), is augmented by the contributions of Eqs. (14) and (15), and is restated as

$$\delta W = \delta W^{\mathrm{int}} + \delta W^{\mathrm{pd}} + \delta W^{\mathrm{pr}} - \delta W^{\mathrm{ext}} = 0 \,. \tag{16}$$

The above equation states the equilibrium condition of virtual work that must be fulfilled for any arbitrary variation of the displacement variables δu_r. Equation (16) is a nonlinear equation system which can be linearized for the purposes of solving the shell problem using the Newton–Raphson method:

$$\frac{\partial^2 W}{\partial u_r \partial u_s} \Delta u_s = -\frac{\partial W}{\partial u_r} \,. \tag{17}$$

The first derivative of the virtual work terms is the residual force vector, whereas the second derivative yields the stiffness matrix. The contributions from the internal and external virtual work are detailed in Kiendl et al. [6]. Here, the first and second derivatives of the penalty virtual work are presented. The derivatives of the displacement penalty virtual work, Eq. (14), are given as follows:

$$\frac{\partial W^{\mathrm{pd}}}{\partial u_r} = \int_{\mathcal{L}} \alpha_{\mathrm{d}} \left(\mathbf{u}^{\mathrm{A}} - \mathbf{u}^{\mathrm{B}}\right) \cdot \left(\mathbf{u}^{\mathrm{A}}_{,r} - \mathbf{u}^{\mathrm{B}}_{,r}\right) \mathrm{d}\mathcal{L} \,, \tag{18}$$

$$\frac{\partial W^{\mathrm{pd}}}{\partial u_r \partial u_s} = \int_{\mathcal{L}} \alpha_{\mathrm{d}} \left(\mathbf{u}^{\mathrm{A}}_{,s} - \mathbf{u}^{\mathrm{B}}_{,s}\right) \cdot \left(\mathbf{u}^{\mathrm{A}}_{,r} - \mathbf{u}^{\mathrm{B}}_{,r}\right) \mathrm{d}\mathcal{L} \,. \tag{19}$$

Similarly, the first and second derivatives of the rotation penalty virtual work, Eq. (15), are

$$\begin{aligned}\frac{\partial W^{\mathrm{pr}}}{\partial u_r} = \int_{\mathcal{L}} \alpha_{\mathrm{r}} \Big(&\left(\mathbf{a}^{\mathrm{A}}_3 \cdot \mathbf{a}^{\mathrm{B}}_3 - \mathring{\mathbf{a}}^{\mathrm{A}}_3 \cdot \mathring{\mathbf{a}}^{\mathrm{B}}_3\right) \left(\mathbf{a}^{\mathrm{A}}_{3,r} \cdot \mathbf{a}^{\mathrm{B}}_3 + \mathbf{a}^{\mathrm{A}}_3 \cdot \mathbf{a}^{\mathrm{B}}_{3,r}\right) \\ &+ \left(\mathbf{a}^{\mathrm{A}}_n \cdot \mathbf{a}^{\mathrm{B}}_3 - \mathring{\mathbf{a}}^{\mathrm{A}}_n \cdot \mathring{\mathbf{a}}^{\mathrm{B}}_3\right) \left(\mathbf{a}^{\mathrm{A}}_{n,r} \cdot \mathbf{a}^{\mathrm{B}}_3 + \mathbf{a}^{\mathrm{A}}_n \cdot \mathbf{a}^{\mathrm{B}}_{3,r}\right) \Big) \mathrm{d}\mathcal{L} \,,\end{aligned} \tag{20}$$

$$\begin{aligned}\frac{\partial W^{\mathrm{pr}}}{\partial u_r \partial u_s} = \int_{\mathcal{L}} \alpha_{\mathrm{r}} \Big(&\left(\mathbf{a}^{\mathrm{A}}_3 \cdot \mathbf{a}^{\mathrm{B}}_3 - \mathring{\mathbf{a}}^{\mathrm{A}}_3 \cdot \mathring{\mathbf{a}}^{\mathrm{B}}_3\right) \left(\mathbf{a}^{\mathrm{A}}_{3,rs} \cdot \mathbf{a}^{\mathrm{B}}_3 + \mathbf{a}^{\mathrm{A}}_{3,r} \cdot \mathbf{a}^{\mathrm{B}}_{3,s} + \mathbf{a}^{\mathrm{A}}_{3,s} \cdot \mathbf{a}^{\mathrm{B}}_{3,r} + \mathbf{a}^{\mathrm{A}}_3 \cdot \mathbf{a}^{\mathrm{B}}_{3,rs}\right) \\ &+ \left(\mathbf{a}^{\mathrm{A}}_{3,s} \cdot \mathbf{a}^{\mathrm{B}}_3 + \mathbf{a}^{\mathrm{A}}_3 \cdot \mathbf{a}^{\mathrm{B}}_{3,s}\right) \left(\mathbf{a}^{\mathrm{A}}_{3,r} \cdot \mathbf{a}^{\mathrm{B}}_3 + \mathbf{a}^{\mathrm{A}}_3 \cdot \mathbf{a}^{\mathrm{B}}_{3,r}\right) \\ &+ \left(\mathbf{a}^{\mathrm{A}}_n \cdot \mathbf{a}^{\mathrm{B}}_3 - \mathring{\mathbf{a}}^{\mathrm{A}}_n \cdot \mathring{\mathbf{a}}^{\mathrm{B}}_3\right) \left(\mathbf{a}^{\mathrm{A}}_{n,rs} \cdot \mathbf{a}^{\mathrm{B}}_3 + \mathbf{a}^{\mathrm{A}}_{n,r} \cdot \mathbf{a}^{\mathrm{B}}_{3,s} + \mathbf{a}^{\mathrm{A}}_{n,s} \cdot \mathbf{a}^{\mathrm{B}}_{3,r} + \mathbf{a}^{\mathrm{A}}_n \cdot \mathbf{a}^{\mathrm{B}}_{3,rs}\right) \\ &+ \left(\mathbf{a}^{\mathrm{A}}_{n,s} \cdot \mathbf{a}^{\mathrm{B}}_3 + \mathbf{a}^{\mathrm{A}}_n \cdot \mathbf{a}^{\mathrm{B}}_{3,s}\right) \left(\mathbf{a}^{\mathrm{A}}_{n,r} \cdot \mathbf{a}^{\mathrm{B}}_3 + \mathbf{a}^{\mathrm{A}}_n \cdot \mathbf{a}^{\mathrm{B}}_{3,r}\right) \Big) \mathrm{d}\mathcal{L} \,.\end{aligned} \tag{21}$$

Equations (20) and (21) require the first and second derivatives of $\mathbf{a}_n$, which are defined below:

$$\mathbf{a}_{t,r} = \frac{1}{\|\tilde{\mathbf{a}}_t\|} \left(\tilde{\mathbf{a}}_{t,r} - \left(\mathbf{a}_t \cdot \tilde{\mathbf{a}}_{t,r}\right) \mathbf{a}_t\right) \,, \tag{22}$$

$$\mathbf{a}_{n,r} = \mathbf{a}_{t,r} \times \mathbf{a}_3 + \mathbf{a}_t \times \mathbf{a}_{3,r} \,, \tag{23}$$

and

$$\begin{aligned}\mathbf{a}_{t,rs} &= -\frac{1}{\|\tilde{\mathbf{a}}_t\|} \left(\left(\mathbf{a}_{t,s} \cdot \tilde{\mathbf{a}}_{t,r}\right) \mathbf{a}_t + \left(\mathbf{a}_t \cdot \tilde{\mathbf{a}}_{t,s}\right) \mathbf{a}_{t,r} + \left(\mathbf{a}_t \cdot \tilde{\mathbf{a}}_{t,r}\right) \mathbf{a}_{t,s}\right) \\ &= -\frac{1}{\|\tilde{\mathbf{a}}_t\|} \left(\mathbf{a}_{t,s} \cdot \tilde{\mathbf{a}}_{t,r}\right) \mathbf{a}_t + \frac{1}{\|\tilde{\mathbf{a}}_t\|^2} \left(2 \left(\mathbf{a}_t \cdot \tilde{\mathbf{a}}_{t,r}\right) \left(\mathbf{a}_t \cdot \tilde{\mathbf{a}}_{t,s}\right) \mathbf{a}_t - \left(\mathbf{a}_t \cdot \tilde{\mathbf{a}}_{t,s}\right) \tilde{\mathbf{a}}_{t,r} - \left(\mathbf{a}_t \cdot \tilde{\mathbf{a}}_{t,r}\right) \tilde{\mathbf{a}}_{t,s}\right) \,,\end{aligned} \tag{24}$$

$$\mathbf{a}_{n,rs} = \mathbf{a}_{t,rs} \times \mathbf{a}_3 + \mathbf{a}_{t,r} \times \mathbf{a}_{3,s} + \mathbf{a}_{t,s} \times \mathbf{a}_{3,r} + \mathbf{a}_t \times \mathbf{a}_{3,rs} \,. \tag{25}$$

Additional details regarding the discretization of the variables used in these expressions can be found in Kiendl et al. [6]. Note that, for the case of patch coupling at patch edges, $\tilde{\mathbf{a}}_t$ is simply $\mathbf{a}_1$ or $\mathbf{a}_2$, depending on the edge ($\mathbf{a}_1$ and $\mathbf{a}_2$ are generally not unit vectors). Thus, the first and

second derivatives of $\tilde{\mathbf{a}}_t$ often correspond to the derivatives of $\mathbf{a}_1$ or $\mathbf{a}_2$. If the penalty formulation is integrated over a trimming curve, it is possible to use the tangent of the trimming curve's projection on the patch as $\tilde{\mathbf{a}}_t$. Trimming is outside the scope of the present work and will be investigated in the future.

Remark 1. Close investigation of Eq. (21) reveals the importance of having complementary terms in Eq. (15). Consider patches forming an angle of 180° wherein the vectors $\mathbf{a}_3^{\mathrm{A}}$ and $\mathbf{a}_3^{\mathrm{B}}$ are parallel. In this situation, the vector derivative $\mathbf{a}_{3,s}^{\mathrm{A}}$ is orthogonal to $\mathbf{a}_3^{\mathrm{B}}$ and, similarly, $\mathbf{a}_{3,s}^{\mathrm{B}}$ is orthogonal to $\mathbf{a}_3^{\mathrm{A}}$; thus, the entire term $\left(\mathbf{a}_{3,s}^{\mathrm{A}} \cdot \mathbf{a}_3^{\mathrm{B}} + \mathbf{a}_3^{\mathrm{A}} \cdot \mathbf{a}_{3,s}^{\mathrm{B}}\right)$ in Eq. (21) would be equal to zero. Furthermore, in geometrically linear analysis and in the first step of geometrically nonlinear analysis, the deformed and undeformed configurations are equivalent and, correspondingly, the terms $\left(\mathbf{a}_3^{\mathrm{A}} \cdot \mathbf{a}_3^{\mathrm{B}} - \mathring{\mathbf{a}}_3^{\mathrm{A}} \cdot \mathring{\mathbf{a}}_3^{\mathrm{B}}\right)$ and $\left(\mathbf{a}_n^{\mathrm{A}} \cdot \mathbf{a}_3^{\mathrm{B}} - \mathring{\mathbf{a}}_n^{\mathrm{A}} \cdot \mathring{\mathbf{a}}_3^{\mathrm{B}}\right)$ are equal to zero. Thus, in this particular configuration, there is zero penalty stiffness contribution from lines one through three of Eq. (21); however, there would still be penalty stiffness contribution from line four of Eq. (21). Conversely, it can be shown that, for configurations wherein patches form an angle of 90°, lines one, three, and four of Eq. (21) have zero penalty stiffness contribution while line two of Eq. (21) has non-zero penalty stiffness contribution. The formulations are therefore complementary throughout a range of possible patch angles.

Remark 2. Equations (18)–(21) can also be used to weakly impose boundary and symmetry conditions on a patch. For restraining the displacement on a boundary of patch $\mathcal{S}^{\mathrm{A}}$ in the case of simply supported or clamped boundary conditions, one can use Eqs. (18) and (19) and set $\mathbf{u}^{\mathrm{B}}$ and its derivatives to zero. For restraining the displacement in the case of a symmetry condition, only the component of $\mathbf{u}^{\mathrm{A}}$ normal to the symmetry plane is considered in the equations. For restraining the rotation in the case of a clamped boundary condition, one can use Eqs. (20) and (21), excluding the second line of (20) and the last two lines of (21), and replacing $\mathbf{a}_3^{\mathrm{B}}$ and $\mathring{\mathbf{a}}_3^{\mathrm{B}}$ by $\mathring{\mathbf{a}}_n^{\mathrm{A}}$. (Note that the terms associated with the derivatives of $\mathbf{a}_3^{\mathrm{B}}$ become zero.) For restraining the rotation in the case of a symmetry condition, $\mathbf{a}_3^{\mathrm{B}}$ and $\mathring{\mathbf{a}}_3^{\mathrm{B}}$ are replaced by the normal vector of the symmetry plane. Finally, in the case of restraining the displacement and rotation of a symmetry condition, the resulting terms from Eqs. (18)–(21) are multiplied by two to correctly represent contributions from both sides of the symmetry plane.

2.3. Implementation

For cases in which the discretization of patches $\mathcal{S}^{\mathrm{A}}$ and $\mathcal{S}^{\mathrm{B}}$ is non-matching along $\mathcal{L}$, there are various possibilities regarding the discretization of $\mathcal{L}$. The discretization of $\mathcal{L}$ can theoretically be entirely independent of the discretizations of both $\mathcal{S}^{\mathrm{A}}$ and $\mathcal{S}^{\mathrm{B}}$. However, for cases which employ patch coupling along patch edges, one might naturally employ the discretization of $\mathcal{S}^{\mathrm{A}}$, $\mathcal{S}^{\mathrm{B}}$, or some combination of the two to construct the penalty terms. For the sake of straightforward

implementation, this work employs the discretization of the patch edge which, across the penalty domain $\mathcal{L}$, has the largest number of elements. For cases in which the discretization of both edges is relatively uniform, this is a conservative choice in that it ensures that the entirety of both edges is penalized. In contrast, if the coarser discretization is selected, it is possible that some of the smaller elements would go unconstrained. Of course, the choice of discretization for $\mathcal{L}$ could impact the results; this represents a future research opportunity. As the examples in later sections demonstrate, however, the simple approach described here is often sufficient.

In other configurations, the interface of patches $\mathcal{S}^{\mathrm{A}}$ and $\mathcal{S}^{\mathrm{B}}$ may not be a patch edge. Instead, $\mathcal{L}$ may be an intersection of two NURBS surfaces. In general, it may not be feasible to determine the mathematically exact intersection of the two surfaces; CAD systems are typically tasked with finding approximate, NURBS-curve representations of such intersections according to system- or user-defined tolerances. In this case, the integration domain $\mathcal{L}$ may be defined by the approximate intersection curve and the discretizations of $\mathcal{L}$, $\mathcal{S}^{\mathrm{A}}$, and $\mathcal{S}^{\mathrm{B}}$ may not correlate. The proposed methodology is still applicable in such circumstances.

When evaluating Eqs. (18)–(21), one must integrate over $\mathcal{L}$ whilst incorporating variables defined on both $\mathcal{S}^{\mathrm{A}}$ and $\mathcal{S}^{\mathrm{B}}$. In the numerical setting, Gaussian quadrature points are defined along $\mathcal{L}$.[2] At each quadrature point on $\mathcal{L}$, variables with superscripts "A" or "B" in the penalty formulations are evaluated at the points on patches $\mathcal{S}^{\mathrm{A}}$ and $\mathcal{S}^{\mathrm{B}}$ which are physically nearest to the quadrature point on $\mathcal{L}$. Note that these nearest points on $\mathcal{S}^{\mathrm{A}}$ and $\mathcal{S}^{\mathrm{B}}$ may not be a quadrature point of the respective patches. For many simple configurations, the corresponding points on $\mathcal{L}$ and the two patches are exactly co-located. For more complex situations (such as the case of non-watertight geometries), the nearest points can be determined using the approach proposed in Bazilevs et al. [23, Section 3.4].

It is also important to properly assemble the contributions of Eqs. (18)–(21) to the global system matrices. This is especially relevant for cases in which the discretization of $\mathcal{L}$ does not match the discretization of one or both of the shell surfaces. In the traditional approach of element-wise assembly, one would first form the element matrices with respect to the elements of $\mathcal{L}$. However, a single element of $\mathcal{L}$ may not correlate with an element in the shells $\mathcal{S}^{\mathrm{A}}$ or $\mathcal{S}^{\mathrm{B}}$, making the assembly impossible. This problem is resolved by simply assembling the contributions of Eqs. (18)–(21) directly at each quadrature point to the global matrices. As described above, each quadrature point on $\mathcal{L}$ is associated with the nearest points on $\mathcal{S}^{\mathrm{A}}$ and $\mathcal{S}^{\mathrm{B}}$. For each quadrature point on $\mathcal{L}$, the basis function information at each of the nearest points on $\mathcal{S}^{\mathrm{A}}$ and $\mathcal{S}^{\mathrm{B}}$ can be employed to directly apply the penalty contributions to the degrees of freedom of the shell problem.

[2] In this work, the full Gauss quadrature rule is used to integrate $\mathcal{L}$. The effect of different quadrature rules and the potential for overconstraining and locking are interesting topics that represent avenues for future research.

2.4. Selection of penalty parameters

A key drawback of penalty methods is that the penalty parameters must be high enough to ensure constraint satisfaction without creating excessive ill-conditioning. The selection of penalty parameters, usually performed empirically by the analyst, has a strong influence on the solution quality. A straightforward strategy is to directly employ a single value for both displacement and rotation penalties:

$$\alpha_{\mathrm{d}} = \alpha_{\mathrm{r}} = \alpha \,, \tag{26}$$

where α is an adjustable penalty parameter. As will be shown, this strategy does not ensure that a given value of α is appropriate for a variety of problem configurations and, in practice, requires user selection of α based on trial and error.

In this work, it is shown that, rather than requiring user selection of the penalty parameters, the parameters can be formulated according to the problem configuration, that is, according to geometry and material properties. A single value of α, scaled by problem-specific parameters, can then be reliably used for various problems. In this work, the displacement and rotation penalty parameters are formulated with respect to the shell membrane and bending stiffnesses, respectively, in order to make the penalty terms dimensionally consistent with the rest of the problem and in order to scale the terms according to kinematically-relevant stiffness properties:

$$\alpha_{\mathrm{d}} = \alpha \frac{\max_{i,j}\left(\mathbb{A}_{ij}\right)}{h} \,, \tag{27}$$

$$\alpha_{\mathrm{r}} = \alpha \frac{\max_{i,j}\left(\mathbb{D}_{ij}\right)}{h} \,, \tag{28}$$

where α is a penalty coefficient, $\mathbb{A}_{ij}$ and $\mathbb{D}_{ij}$ are the membrane and bending stiffnesses given in Eqs. (10) and (12), respectively, $h = \left(h^{\mathrm{A}} + h^{\mathrm{B}}\right)/2$, h^{A} and h^{B} are the lengths of the local elements in the direction most parallel to the penalty curve, $i = 1, 2$, and $j = 1, 2$. For uniform isotropic configurations, the expressions reduce to

$$\alpha_{\mathrm{d}} = \alpha \frac{E\,t}{h\,(1-\nu^2)} \,, \tag{29}$$

$$\alpha_{\mathrm{r}} = \alpha \frac{E\,t^3}{12\,h\,(1-\nu^2)} \,, \tag{30}$$

where E is Young's modulus, t is the shell thickness, and ν is Poisson's ratio.

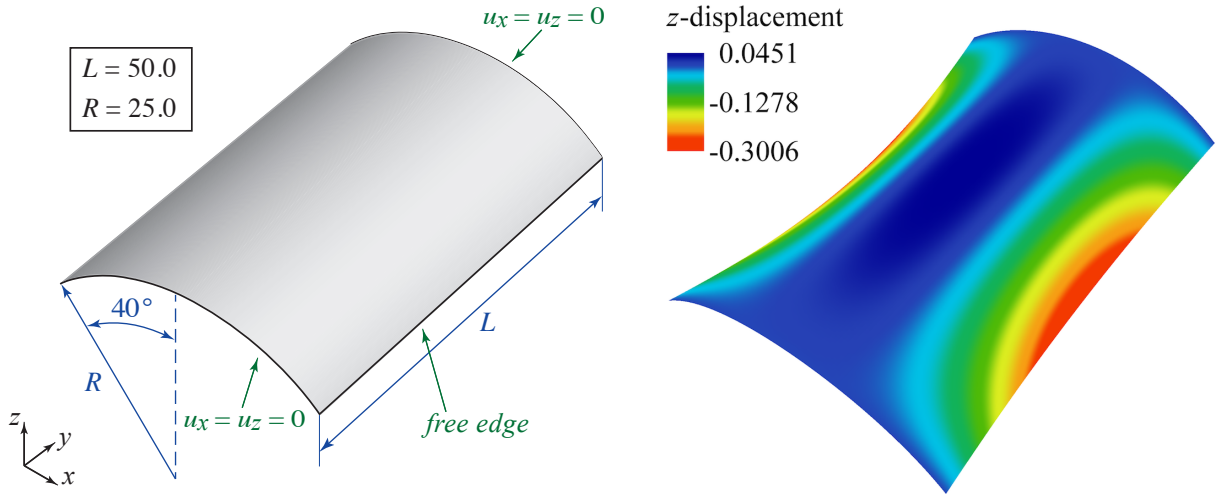

Figure 4: Scordelis–Lo roof problem description and deformation (scaled by a factor of 10 for visualization).

3. Benchmark examples

A variety of geometrically linear and nonlinear benchmark examples are employed to explore the behavior of the coupling methodology and the formulations for the penalty parameters proposed in Eqs. (27) and (28). Examples featuring different geometries, material properties, and analysis types are selected, and a combination of matching and non-matching discretization strategies are used throughout, all to demonstrate the effectiveness and flexibility of the method. The appropriate range for the dimensionless penalty coefficient, α, is also explored. The geometrically linear analyses are done by performing only one iteration step of the nonlinear analysis. Linear systems are solved using direct solvers, eigenvalue problems are solved using a SLEPc-based Krylov–Schur solver [24, 25], and the highly nonlinear examples in Sections 3.6 and 3.7 employ the modified Riks (arc length) method [26].

3.1. Scordelis–Lo roof

The Scordelis–Lo roof is a geometrically linear problem from the well-known shell obstacle course proposed by Belytschko et al. [27] to test accuracy and robustness in complex strain states. The problem configuration and dimensions of the geometry are shown in Figure 4. The ends of the geometry are supported by rigid diaphragms while the remaining edges are left unconstrained. A uniform gravitational load of 90.0 per unit area is applied to the roof, and the resulting linear deformation is quantified by evaluating the vertical displacement of the midpoint of the free edge. For the benchmark problem, the thickness and Young's modulus of the roof are $t = 0.25$ and $E = 4.32 \times 10^8$, respectively. Figure 4 also shows the deformation of the roof.

The geometry of the Scordelis–Lo roof is modeled using multiple NURBS patches of degree 3 with both matching and non-matching discretizations as shown in Figures 5a and 5b, respectively.

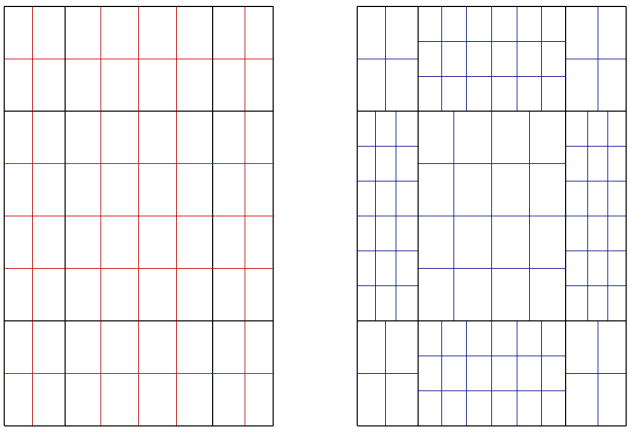

(a) Matching (b) Non-matching

Figure 5: Meshes for the matching and non-matching configurations of the Scordelis–Lo roof. Thick black lines indicate patch boundaries.

For the purpose of exploring the effective range of α, the deformation of both the matching and non-matching cases is calculated using the proposed penalty parameter formulations, Eqs. (27) and (28), and the α-only formulation, Eq. (26), over a range of values of α. This same study is repeated for cases wherein the shell thickness, t, and Young's modulus, E, have been modified. Throughout these studies, analyses are performed using the meshes shown in Figures 5a and 5b with two levels of h-refinement; the meshes in Figure 5 will be used for the convergence study presented later.

The results of the analyses performed using the benchmark material parameters are shown for the proposed penalty formulations in Figure 6a and for the α-only penalty formulations in Figure 6b. The displacements are normalized by a converged reference value, $u_z = -3.005925 \times 10^{-1}$, obtained using a single-patch model discretized with 128×128 bicubic elements. As expected, the results in both cases indicate a range of values of α for which the penalty coupling methodology is effective and produces the correct result. Also note that accurate results are obtained for both the matching and non-matching cases. These results clearly show that, if the value of the penalty parameter is too low, the patch coupling constraint is not enforced. If the penalty parameter value is too high, the matrices may become ill-conditioned and the solution of the linear system is prone to large numerical errors. Both scenarios lead to solutions deviating from the reference results. For this reason, we recommend using a penalty value that is sufficiently high to produce an accurate result but no higher than necessary.

The results in Figures 6a and 6b alone do not indicate the importance of the proposed penalty formulations. The value can be understood, however, upon performing the same analysis with different sets of material parameters. The results obtained using a thickness of $t = 0.025$ instead of $t = 0.25$ are shown for the proposed and α-only formulations in Figures 6c and 6d, respectively. The displacements are normalized by a converged reference value of $u_z = -32.01045$, obtained us-

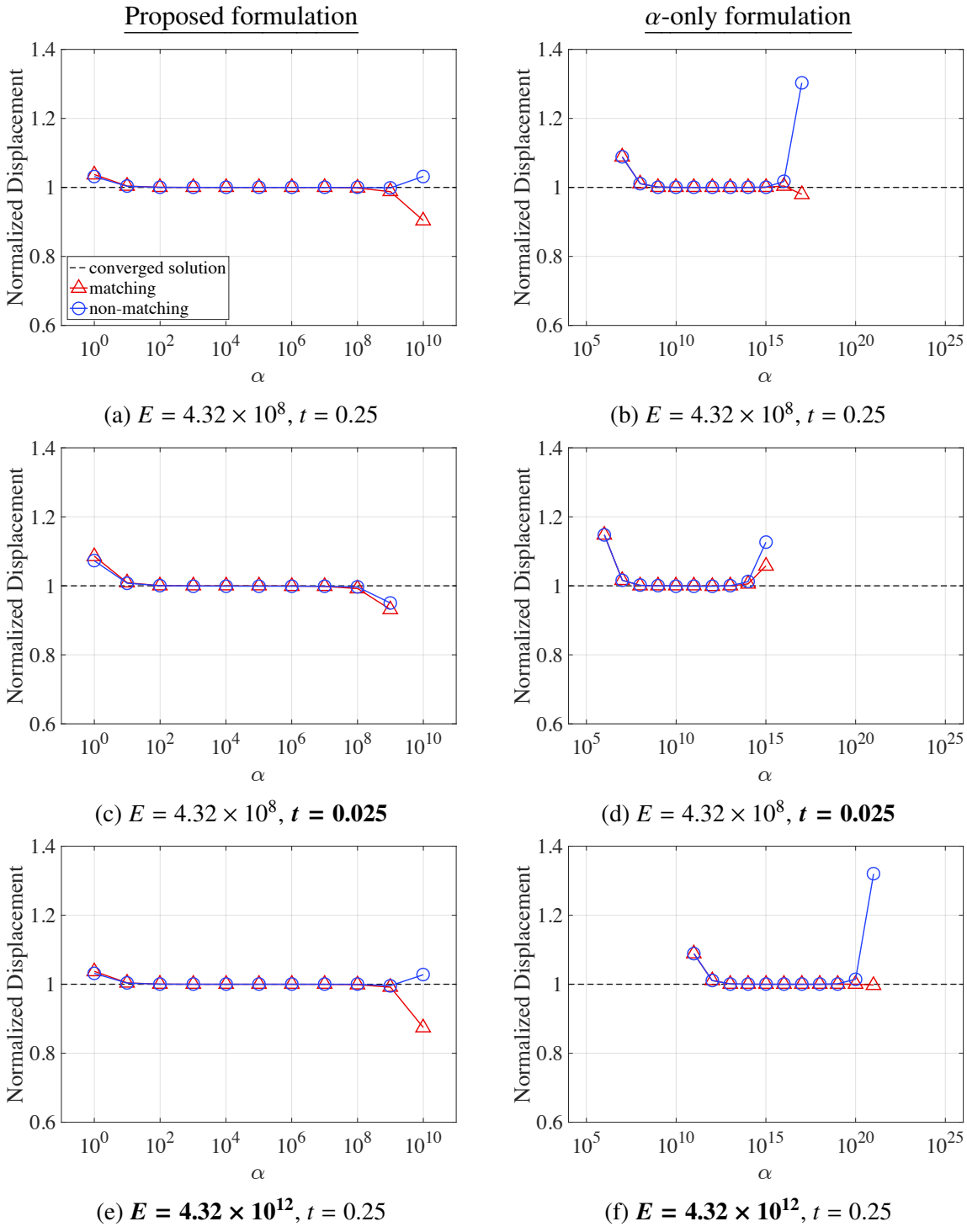

(a) $E = 4.32 \times 10^8$, $t = 0.25$

(b) $E = 4.32 \times 10^8$, $t = 0.25$

(c) $E = 4.32 \times 10^8$, $\boldsymbol{t = 0.025}$

(d) $E = 4.32 \times 10^8$, $\boldsymbol{t = 0.025}$

(e) $\boldsymbol{E = 4.32 \times 10^{12}}$, $t = 0.25$

(f) $\boldsymbol{E = 4.32 \times 10^{12}}$, $t = 0.25$

Figure 6: Vertical displacement at midpoint of the free edge of the Scordelis–Lo roof, normalized with respect to the converged reference value, with varying penalty value α using the proposed penalty approach and the α-only approach for both matching and non-matching discretizations and different combinations of setup variables.

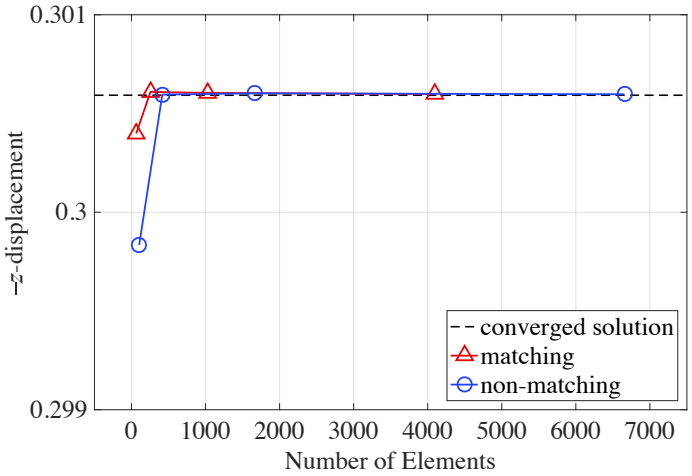

Figure 7: Vertical displacement at midpoint of the free edge of the Scordelis–Lo roof under h-refinement for the proposed penalty approach with $\alpha = 10^3$.

ing the same single-patch mesh as before. Similarly, the results obtained using a Young's modulus of $E = 4.32\times10^{12}$ instead of $E = 4.32\times10^{8}$ are shown for the proposed and α-only formulations in Figures 6e and 6f, respectively. The displacements are normalized by a converged reference value of $u_z = -3.005925 \times 10^{-5}$, obtained from a single-patch simulation.

For the cases employing the α-only penalty formulation, shown in Figures 6b, 6d, and 6f, the range of values of α that produce accurate results shifts significantly, by as much as five orders of magnitude, when the problem parameters are changed. This illustrates one of the key drawbacks of penalty methods: because the effective range of α is problem-dependent, an analyst would be forced to select the penalty parameter based on experience. In contrast, for the cases employing the proposed penalty formulations, shown in Figures 6a, 6c, and 6e, the effective range of α remains consistent for all problem configurations. Specifically, an accurate range of approximately $\alpha = 10^2$ to $\alpha = 10^8$ is observed. Thus, a value of $\alpha = 10^3$ is recommended; this value is high enough to reliably produce correct results, but is no higher than necessary.

Solution convergence under mesh refinement can also be demonstrated using the proposed penalty approach. Results are compared to the converged displacement from the single-patch simulations. The coarsest geometries for the matching and non-matching multi-patch configurations are shown in Figures 5a and 5b, and refinement is performed via global h-refinement. All analyses use $\alpha = 10^3$. The results in Figure 7 indicate satisfactory convergence for both the matching and non-matching cases.

3.2. Simply supported plate under sinusoidal load

A simply supported plate problem is employed to study the convergence and conditioning behavior of the proposed penalty approach. The setup for this problem is shown in Figure 8. The

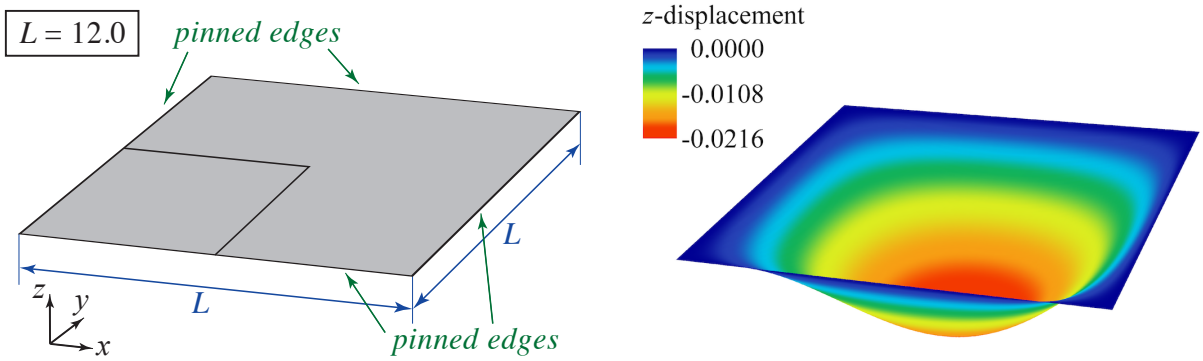

Figure 8: Simply supported plate problem description and deformation (scaled by a factor of 200 for visualization).

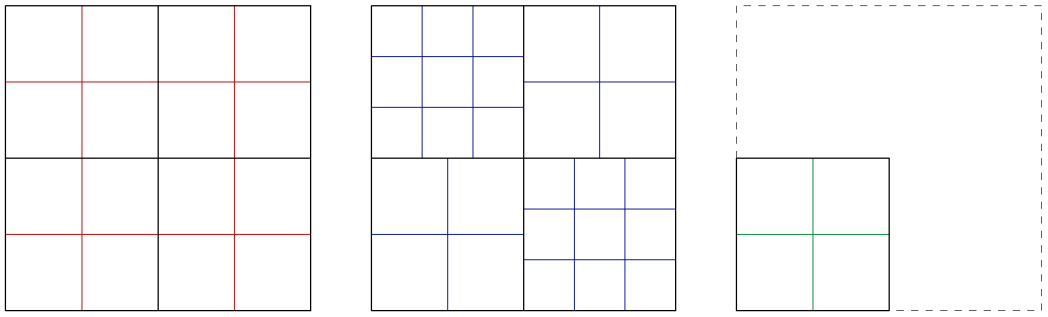

(a) Matching (b) Non-matching (c) Quarter

Figure 9: Meshes for the matching and non-matching full geometry configurations and the quarter geometry configuration of the simply supported plate.

square plate is subjected to a sinusoidal pressure load of $p(x, y) = p_0 \sin(\pi x/L) \sin(\pi y/L)$. The example and results included here utilize a plate with $L = 12.0$, thickness $t = 0.375$, Young's modulus $E = 4.8 \times 10^5$, Poisson's ratio $\nu = 0.38$, and load amplitude $p_0 = 1.0$. The plate deformation is evaluated at the center of the plate, the location of maximum displacement, and is compared to the analytical solution [28],

$$u_{\max} = \frac{p_0 L^4}{4\pi^4 D}, \text{ where } D = \frac{Et^3}{12(1-\nu^2)}. \tag{31}$$

The deformation of the plate is also shown in Figure 8.

To evaluate the performance of the penalty approach for patch coupling and for imposing symmetry conditions, a variety of configurations of this problem are considered. A full plate geometry with four NURBS patches of degree 3 is used to assess patch coupling, while a quarter plate geometry with a single patch of degree 3 is used to assess the enforcement of symmetry conditions. In the full plate geometry, both matching and non-matching mesh configurations are investigated, as shown in Figures 9a and 9b, respectively. Figure 9c shows the mesh configuration of the quarter

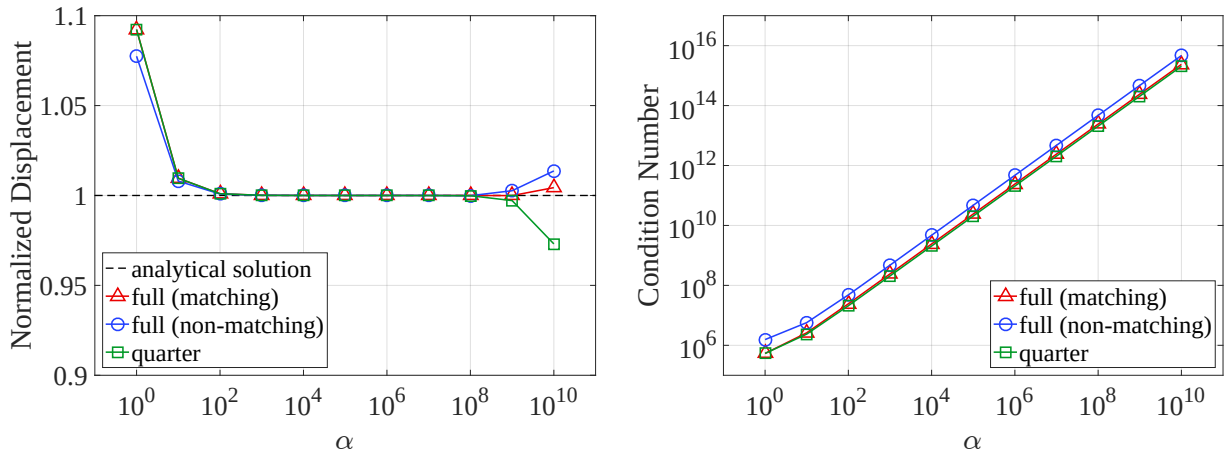

Figure 10: Normalized displacement at the plate center and condition number of the stiffness matrix with varying α.

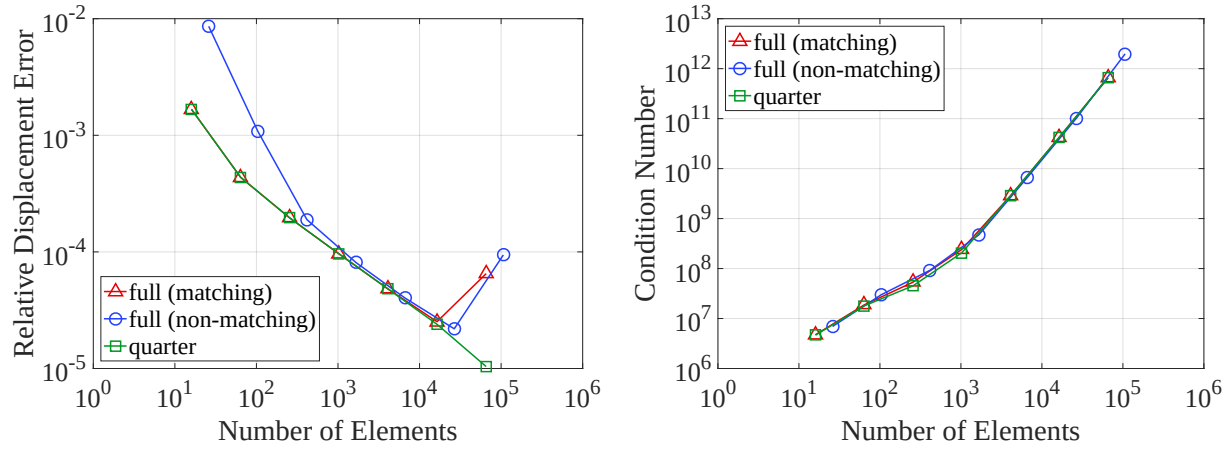

Figure 11: Relative error of the displacement at the plate center and condition number of the plate stiffness matrix under h-refinement with $\alpha = 10^3$. The number of elements for the quarter patch results is scaled by four for comparison.

plate geometry.

For each analysis, the displacement at the center of the plate and the condition number of the stiffness matrix are calculated. Results for both displacement and condition number with varying α are shown in Figure 10. These results use the meshes shown in Figure 9 with three levels of h-refinement. The displacement values indicate the same effective range of α demonstrated in Section 3.1 for each configuration, while the condition number increases with α as expected. The convergence of the displacement and condition number are also studied for the plate under h-refinement, as shown in Figure 11. All convergence results are computed with $\alpha = 10^3$, and the number of elements in the quarter plate configurations is scaled by four for comparison with the full plate geometry. The refinement study highlights the fact that the condition number increases

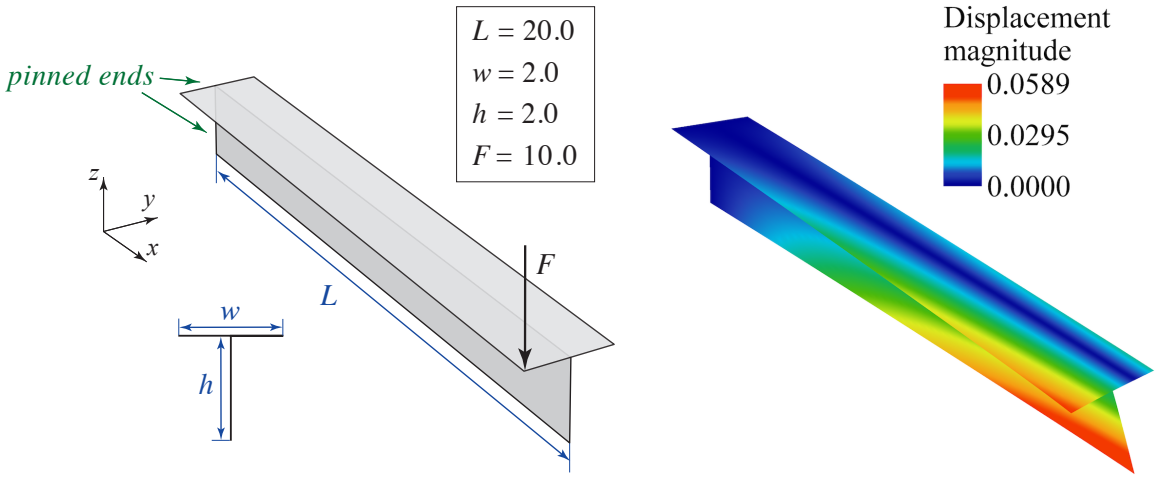

Figure 12: T-beam problem description and deformation (scaled by a factor of 10 for visualization).

with refinement. While this feature helps with overall solution convergence under refinement, it also dictates that, for some cases with excessive refinement, the results may deteriorate.

3.3. T-beam

Complex shell structures typically also include non-smooth patch interfaces, i.e., patches joined with a certain angle; the angle between the patches must be maintained during deformation analysis. An example of this is a T-beam, as depicted in Figure 12. The T-beam is modeled using two planar geometries which are orthogonal at their interface. As shown in Figure 12, one end of the beam is pinned and a force of $F = 10.0$ is applied to one corner of the opposite end in the $-z$ direction. Figure 12 also indicates the dimensions of the geometry. The patches have a Young's modulus of $E = 1.0 \times 10^7$, a thickness of $t = 0.1$, and a Poisson's ratio of $\nu = 0.0$. The deformed geometry is shown in Figure 12.

The T-beam is modeled using two NURBS patches of degree 3. Again, both matching and non-matching mesh configurations are constructed as shown in Figures 13 and 14. For the analyses considered here, two h-refinements are performed on each of the meshes shown in Figures 13 and 14. The geometrically linear analysis is performed, and the angle between the patches at the end of the beam is calculated. If the patches have been properly coupled, an angle of 90° should be maintained. The left side of Figure 15 shows the resultant angle between the two patches for both the matching and non-matching cases for a range of α values. Note that, for relatively low values of α, the structure is effectively unconstrained at its interface, resulting in an angle of approximately 93.5° between the patches. However, in the range of approximately $\alpha = 10^{-2}$ to $\alpha = 10^2$ the constraint begins to take effect, resulting in the desired angle of 90° between the patches for $\alpha > 10^2$. Again, a wide range of acceptable values of α is observed; the range is similar to those observed in the previous examples. Thus, the suggested value of $\alpha = 10^3$ remains

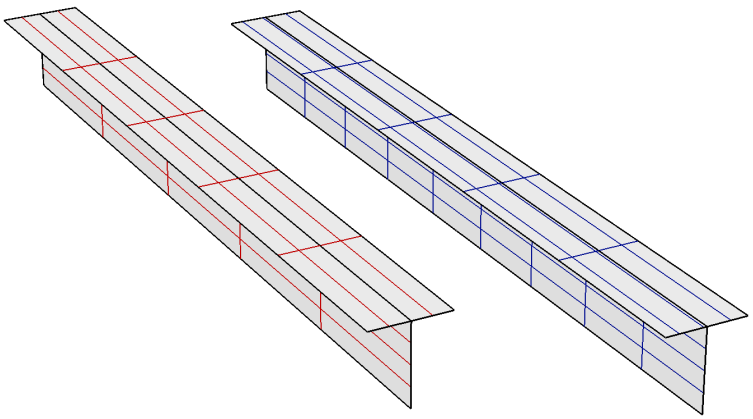

Figure 13: Meshes for the matching (left) and non-matching (right) configurations of the T-beam problem.

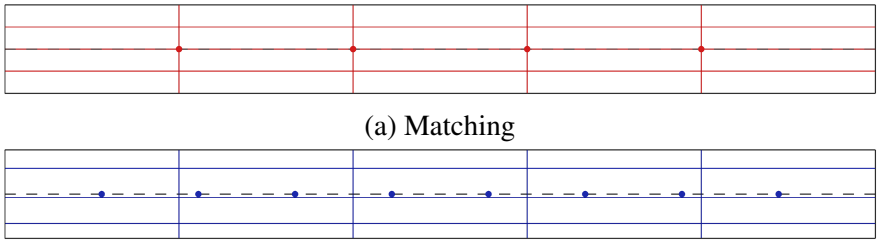

(a) Matching

(b) Non-matching

Figure 14: Top view of meshes for the matching and non-matching configurations of the T-beam problem. Circular markers indicate discretization of perpendicular patch.

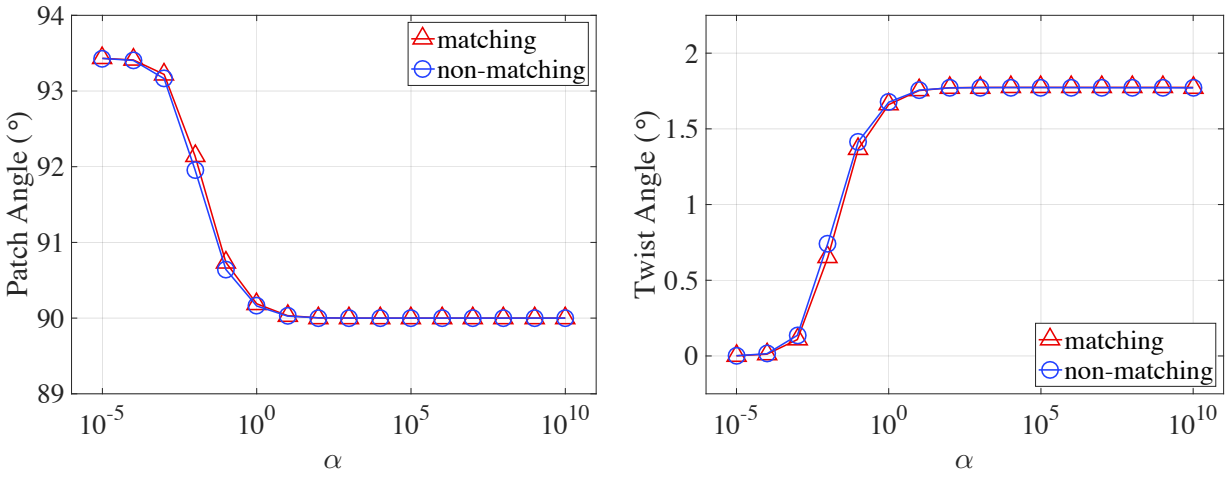

Figure 15: Angle between patches of the T-beam (left) and total twist at the end of the vertical patch (right) with varying penalty value α for both matching and non-matching configurations.

appropriate in this case.

The right side of Figure 15 shows the total twist at the free end of the T-beam measured using the vertical patch. When the penalty value is too low, the patches are effectively uncoupled and the

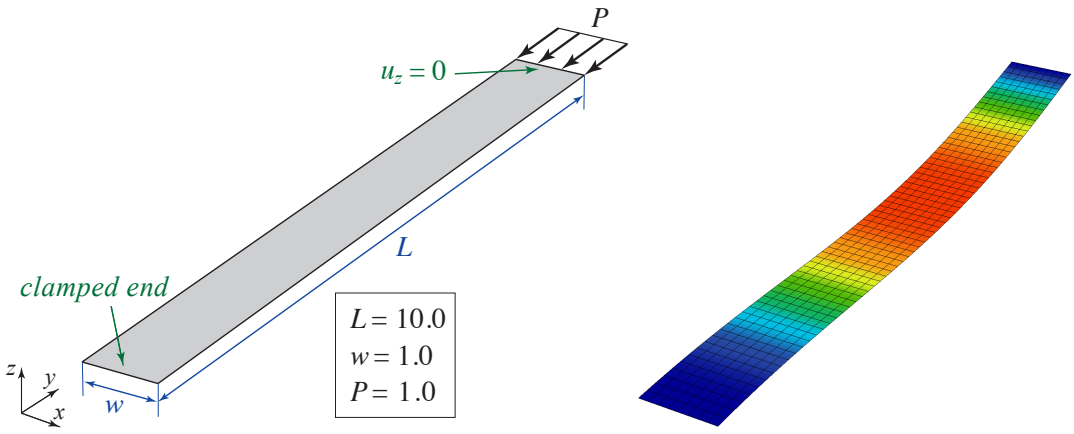

Figure 16: Plate buckling problem description and the deformation for the first buckling mode (color contour indicates relative displacement magnitude).

strain energy is not transferred to the vertical patch, resulting in a twist angle of zero degrees. As the penalty value increases, a consistently reasonable twist angle is observed. Similar results are obtained for both the matching and non-matching configurations.

3.4. Plate buckling

Another important type of analysis that is commonly performed in the design of shell structures, such as wind turbine blades, is linear buckling analysis. Thus, the performance of the proposed penalty formulation is also explored in the context of linear buckling. Linear buckling analysis, or eigenvalue buckling analysis, entails solving the equation

$$\left(\mathbf{K}^{\text{lin}} + \lambda_i \mathbf{K}_{\text{g}}\right) \mathbf{v}_i = 0 \,, \tag{32}$$

where $\mathbf{K}^{\text{lin}}$ is the linear stiffness matrix of the structure, $\mathbf{K}_{\text{g}}$ is the geometric stiffness matrix based on the applied load, and λ_i is the i^{th} eigenvalue associated with mode vector $\mathbf{v}_i$. In this context, an eigenvalue λ_i is a scalar multiplier of the applied loads that will, in theory, cause buckling of the structure; $\mathbf{v}_i$ is the corresponding buckling mode shape.

A plate is employed in a simple buckling configuration, as shown in Figure 16, with one end clamped and the other supported in the vertical direction. The problem is modeled using both matching and non-matching multi-patch configurations. All of the patches are bicubic NURBS surfaces. The discretization of the patches is shown in Figure 17. The patch sizes are intentionally selected such that the patch boundaries do not occur on axes of symmetry. This makes the problem more difficult because, if the penalty does not function properly, it may produce a non-symmetric result. For this problem, Young's modulus is $E = 1.0 \times 10^3$, Poisson's ratio is $\nu = 0.0$, thickness is $t = 0.1$, and the applied distributed force is $P = 1.0$ in terms of force per unit length.

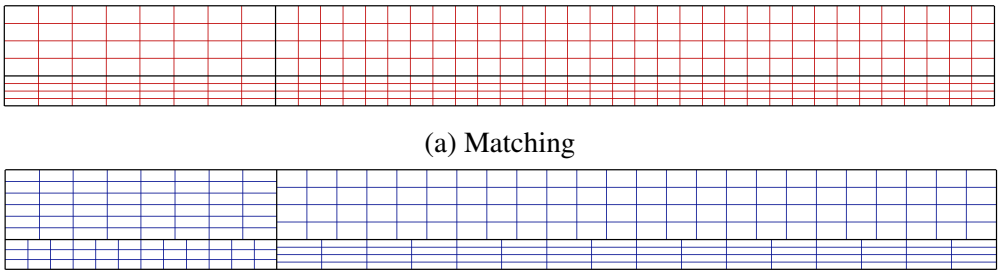

(a) Matching

(b) Non-matching

Figure 17: Meshes for the matching and non-matching configurations of the plate buckling problem.

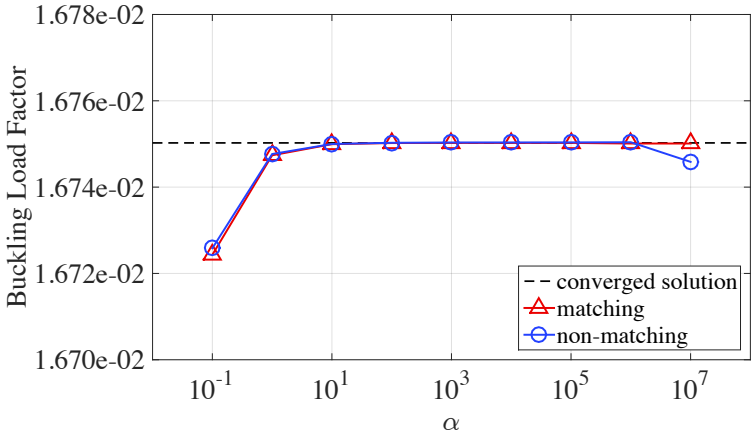

Figure 18: Buckling load factor with varying α for both matching and non-matching configurations of the plate buckling problem.

The plot in Figure 18 indicates that, for a similar range of α parameters observed in the previous problems, the multi-patch configurations produce buckling load factors of sufficient accuracy when compared to a converged result obtained using a single-patch configuration. This illustrates the accuracy of the proposed formulation in the context of linear buckling analysis. Also note that the suggested value of $\alpha = 10^3$ is appropriate here.

3.5. Nonlinear slit annular plate

All of the examples considered thus far have employed linear analysis. However, the presented methodology is also applicable in the geometrically nonlinear setting. Sze et al. [29] identified and reproduced a number of common benchmark problems for nonlinear analysis, one of which is a slit annular plate subjected to a lifting line force. The slit annular plate problem is reproduced using multi-patch models to verify the proposed coupling methodology in the nonlinear setting.

The slit annular plate setup and deformation are illustrated in Figure 19. One side of the slit is clamped, while the other is allowed to freely deform under the applied distributed force, P. The deformation is quantified by tracking the vertical displacement of points A and B, identified in

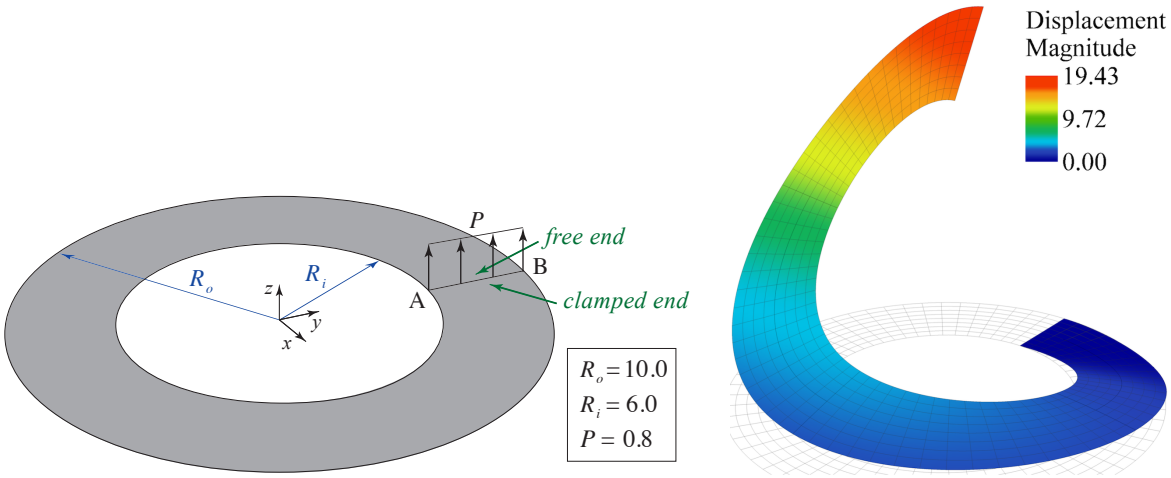

Figure 19: Nonlinear slit annular plate problem description and deformation.

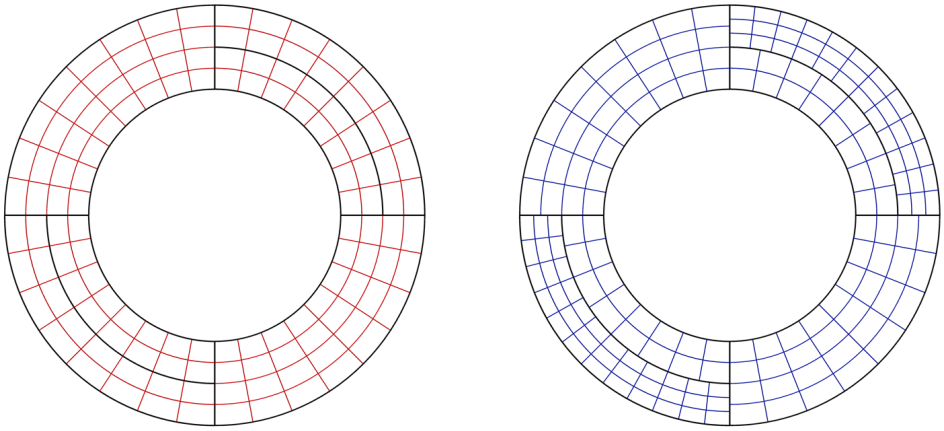

(a) Matching (b) Non-matching

Figure 20: Meshes for the matching and non-matching cases of the nonlinear slit annular plate. Thick black lines indicate patch boundaries.

Figure 19, at incremental loads up to $P = 0.8$. Young's modulus is $E = 21.0 \times 10^6$, thickness is $t = 0.03$, and Poisson's ratio is $\nu = 0.0$.

Refinement studies are not typically performed for the slit annular plate problem in the literature. However, because cases with different discretizations are considered in this work, a refinement study is performed for both matching and non-matching configurations to ensure that the results are comparable. For all of the cases, cubic NURBS patches are employed. The coarsest meshes used in the refinement study are shown in Figure 20, and the displacement of point B due to the the maximum load of $P = 0.8$ under h-refinement is shown in Figure 21. For this analysis, the recommended value of $\alpha = 10^3$ is employed. Convergence is achieved with approximately two h-refinements for both the matching and non-matching cases. Thus, these levels of refinement are used for the following verification of α.

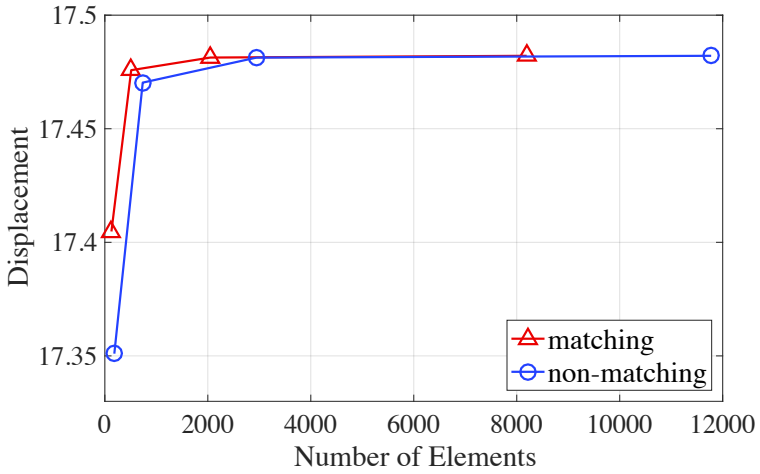

Figure 21: Vertical displacement at point B of the slit annular plate under h-refinement for both matching and non-matching configurations.

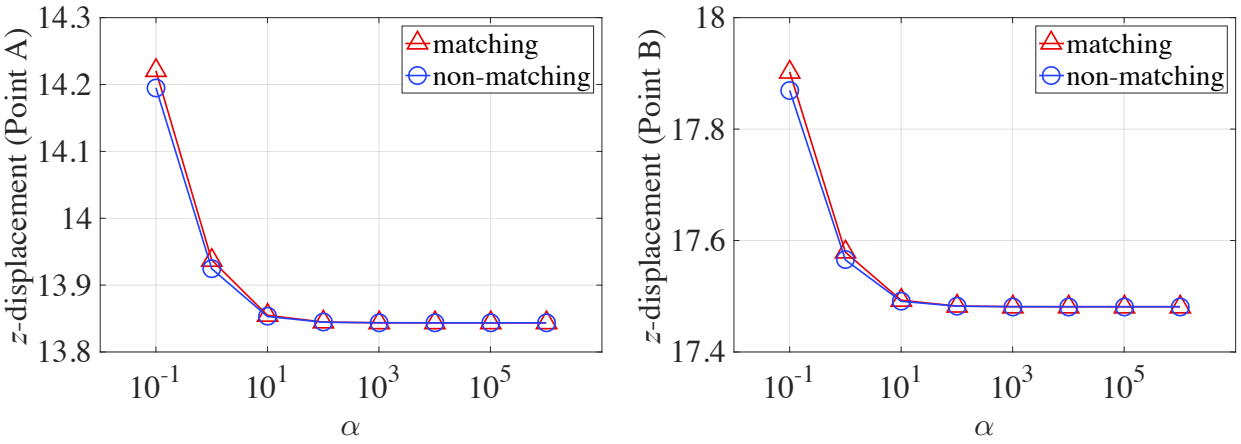

Figure 22: Vertical displacement at points A and B of the slit annular plate due to the maximum applied P for varying values of α.

Figure 22 shows the displacements at A and B for the maximum load of $P = 0.8$ and a range of α values. The accuracy of the method is clearly demonstrated for $\alpha = 10^2$ through $\alpha = 10^6$, with identical results obtained in both the matching and non-matching cases. In nonlinear analysis, a badly conditioned problem is more likely to exhibit divergent behavior, as is the case for $\alpha \geq 10^7$ for this problem. Still, the problem is tractable for a wide range of values of α, and the acceptable range is similar to the range observed in the previous examples. The suggestion of $\alpha = 10^3$ remains appropriate.

Figure 23 shows the displacements of point A and point B under varying applied forces both for the presented methodology and as reported by Sze et al. [29] using a 6×30 mesh of four-node S4R elements in ABAQUS [30]. A penalty coefficient of $\alpha = 10^3$ is used for this comparison, and good agreement with the reference results is observed over the entirety of the load spectrum.

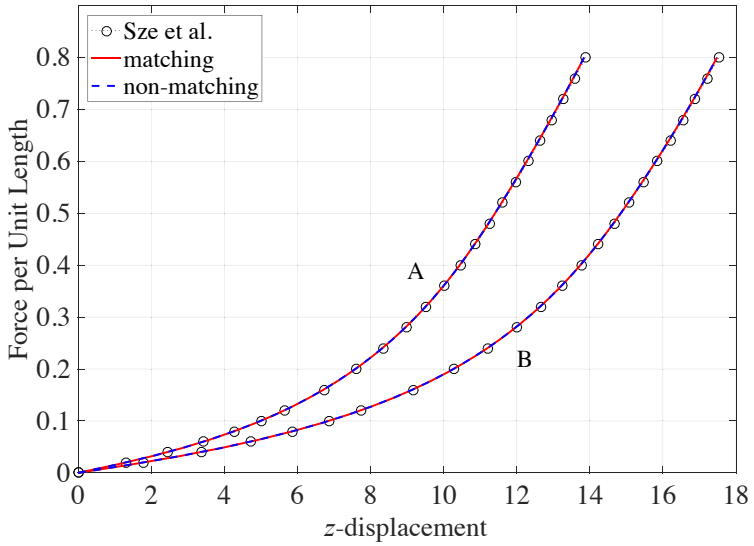

Figure 23: Vertical displacement of points A and B versus applied distributed load for the nonlinear slit annular plate with $\alpha = 10^3$.

3.6. Nonlinear pinched semi-cylindrical shell

The proposed methodology, and in particular the penalty parameter formulations (27) and (28), were also designed to accommodate composite materials. Here, the performance of the proposed method is investigated using a nonlinear pinched semi-cylinder example, shown in Sze et al. [29], featuring isotropic and laminated materials. Figure 24 illustrates the setup and the deformation of the problem. The semi-cylindrical shell is subject to a point load at the middle of the free end of the cylinder. The other end is fully clamped. Along its longitudinal edges, the vertical displacement and the rotation about the y-axis are constrained. For the isotropic configuration, material parameters are $E = 2.0685 \times 10^7$ and $\nu = 0.3$, while for the laminated configuration $E_L = 2.0685 \times 10^7$, $E_T = 0.517125 \times 10^7$, $G_{LT} = 0.7956 \times 10^7$, and $\nu_{LT} = \nu_{TT} = 0.3$. Ply configurations of [0/90/0] and [90/0/90] are used, with each ply having a thickness of $t = 0.01$. The total shell thickness is $t = 0.03$ for all cases. The applied load of $F = 2000$ is scaled by the load factor λ, where $0 < \lambda \leq 1$.

Due to symmetry, the problem is solved by modeling only one half of the structure. The boundary and symmetry conditions are imposed using the proposed penalty approach. Both a single-patch configuration and a non-matching multi-patch configuration are considered to highlight the formulations' performance in the context of nonlinear analysis of composite shells. In both cases, quadratic NURBS patches are used. The two configurations are shown in Figure 25. Note that the multi-patch model includes penalties for clamping, symmetry, and non-matching patch coupling.

Displacements at the location of the applied load under the full load of $F = 2000$ are shown

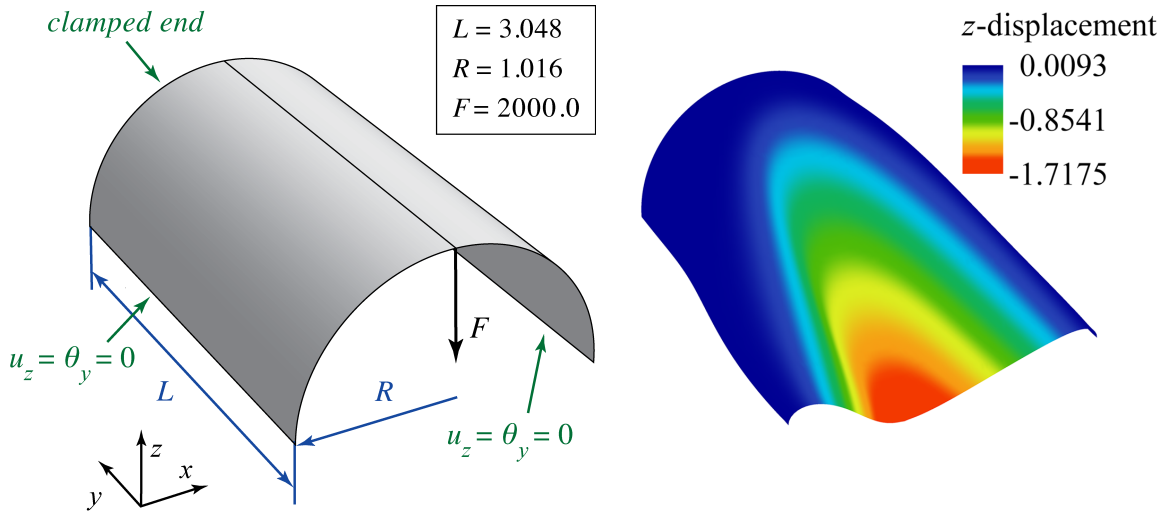

Figure 24: Nonlinear semi-cylinder problem description and deformation at the maximum applied load for the isotropic material case.

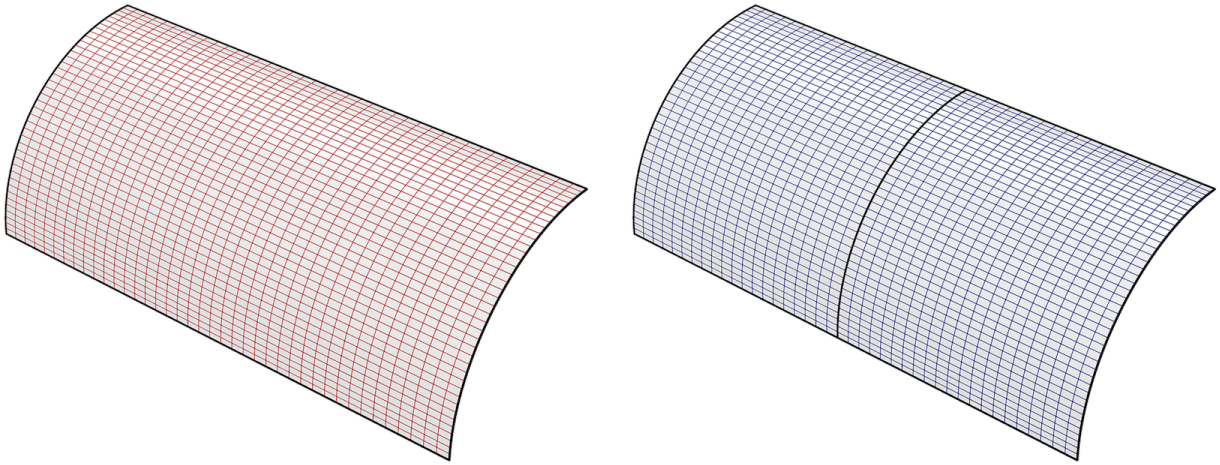

(a) Single patch

(b) Non-matching multi-patch

Figure 25: Meshes for the single-patch and non-matching multi-patch cases of the half geometry of the semi-cylinder. Thick black lines indicate patch boundaries.

for the multi-patch model over a range of penalty parameter values in Figure 26. The results are consistent between $\alpha = 10^2$ and $\alpha = 10^5$, demonstrating the stability of the proposed methodology and confirming the choice of the penalty coefficient of $\alpha = 10^3$. The displacements at the location of the applied load for varying load levels and using $\alpha = 10^3$ are shown in Figure 27. Good agreement with the reference results [29] is observed for all discretizations and material configurations considered, indicating the effectiveness of the proposed method even for nonlinear composite applications.

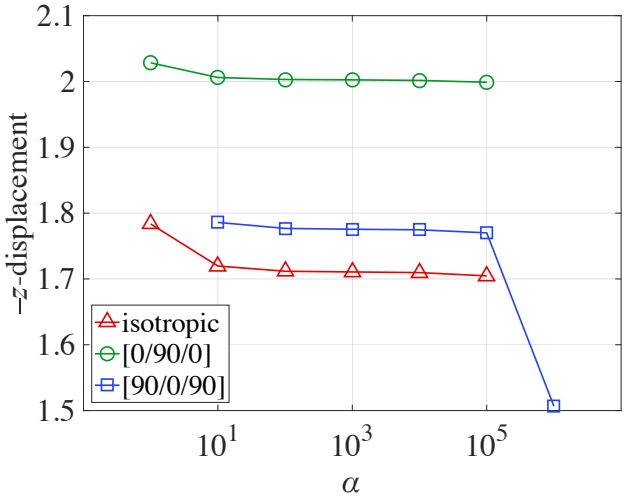

Figure 26: Vertical displacements at the point where the load is applied for the nonlinear semi-cylinder at the maximum load for varying α. The study is performed for the non-matching multi-patch model. The simulations did not converge at $\alpha = 10^6$ for the isotropic and [0/90/0] cases, and at $\alpha = 10^0$ for the [90/0/90] case.

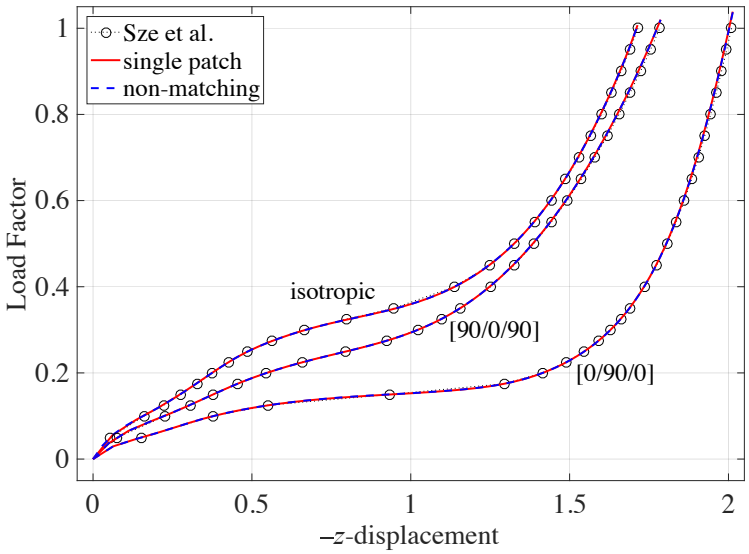

Figure 27: Load factor versus vertical displacement for the nonlinear semi-cylinder problem with $\alpha = 10^3$.

3.7. Hinged cylindrical shallow roof

To further demonstrate the effectiveness of the proposed penalty formulation for challenging, nonlinear problems, the approach is applied to the hinged cylindrical shallow roof [29], a structure involving challenging snap-through and snap-back behaviors in both isotropic and laminated configurations. The problem description and the dimensions of the shallow roof are shown in Figure 28. The shell structure has hinged supports along two edges and is subjected to a concentrated

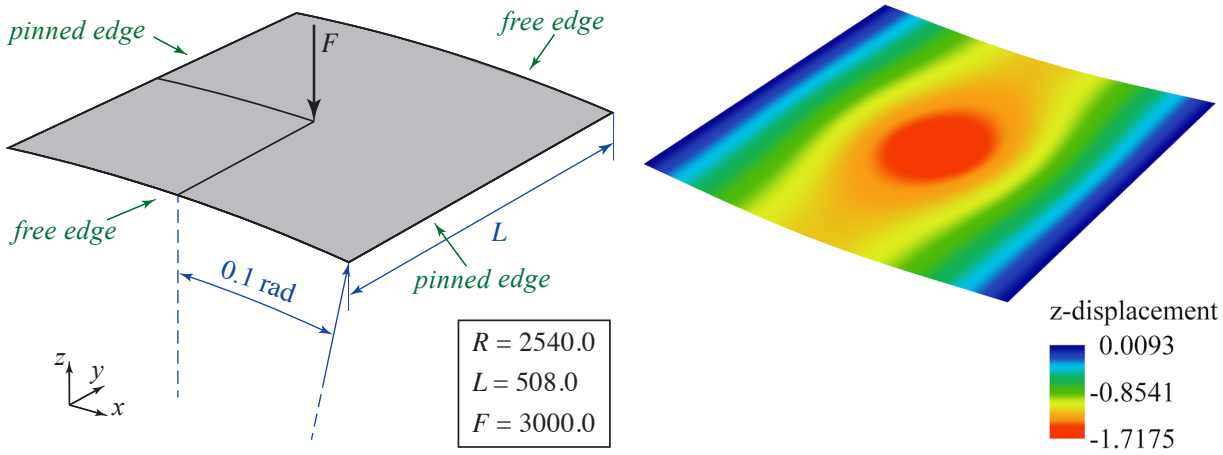

Figure 28: Shallow roof problem description and deformation at the maximum applied load for the isotropic material case.

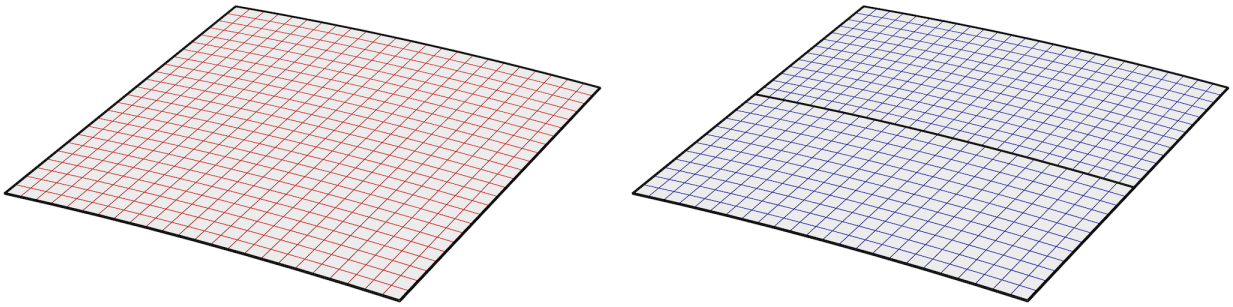

(a) Single patch

(b) Non-matching multi-patch

Figure 29: Meshes for the single patch and non-matching multi-patch cases of the quarter geometry of the shallow roof. Thick black lines indicate patch boundaries.

load up to $F = 3000$. Both isotropic material ($E = 3102.75$, $\nu = 0.3$) and laminated material ($E_L = 3300$, $E_T = 1100$, $G_{LT} = 660$, $\nu_{LT} = \nu_{TT} = 0.25$) are considered; in the case of laminated material, two different ply configurations, [0/90/0] and [90/0/90], are considered. All plies are equal in thickness, having a total shell thickness of $t = 6.35$.

Due to symmetry, only a quarter of the structure is modeled and symmetry conditions are applied with the proposed penalty formulation. As in the previous example, both single-patch and non-matching multi-patch configurations are considered for the quarter geometry (Figure 29), employing bivariate NURBS of degree 2. The load F is scaled by the load factor λ ($0 < \lambda \leq 1$) and applied incrementally up to the maximum value of 3000.

Figure 30 shows the displacement of the central point under the maximum load for different α values. This study is performed for the non-matching multi-patch model featuring one quarter of the structure with patch coupling and symmetry conditions applied using the penalty method. The trend of the results is similar to those of the previous analyses; non-convergence is observed for

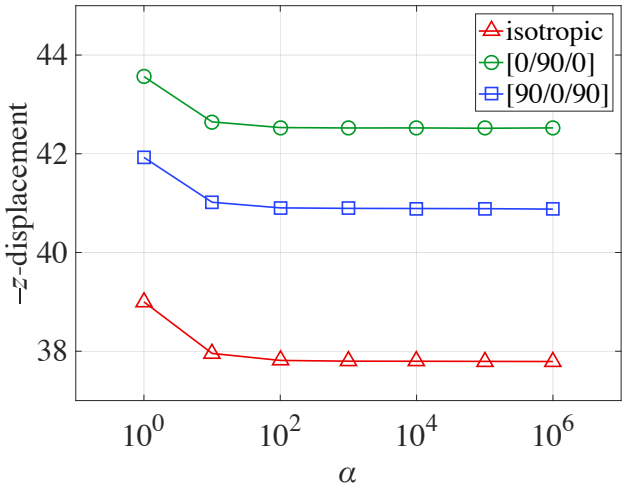

Figure 30: Vertical displacement of the central point of the shallow roof under the maximum load for various values of the penalty parameter α. The study is performed for the non-matching multi-patch model featuring one quarter of the structure.

high values of the penalty parameter, due to poor conditioning, while stable results are obtained for $10^2 \leq \alpha \leq 10^6$.

The results of the nonlinear simulations for the isotropic and laminated cases throughout the load range and for both discretization strategies are shown in Figure 31. The results show good agreement with the reference solutions [29]. Furthermore, the results confirm the validity of the proposed formulation and $\alpha = 10^3$ for highly nonlinear problems, including complex snap-through and snap-back situations, for both isotropic and laminated materials.

4. Application to wind turbine blade analysis

Wind turbine blade design and analysis is an example of a field in which the use of isogeometric Kirchhoff–Love shell analysis could be especially advantageous. Due to the complexity of wind turbine blade structures and the wide range of conditions they must withstand, thorough blade design is a highly iterative process that is governed, in part, by workflow automation and analysis efficiency, both of which may be improved through the application of IGA. The isogeometric Kirchhoff–Love shell formulation has been shown to accurately capture the dynamic kinematic behavior of wind turbine blades [31, 32]. This formulation has also been employed for numerous fluid–structure interaction (FSI)-based analyses of full-scale wind turbines [20, 23, 33–35] and for IGA-based parametric design and optimization of a simplified blade design [36, 37]. The blades in the aforementioned work were modeled using a single-patch NURBS or T-spline surface, or multiple matching NURBS patches coupled using the bending strip method. In this work, a complex 5 MW blade design with shear webs and discontinuous composite definitions is modeled using

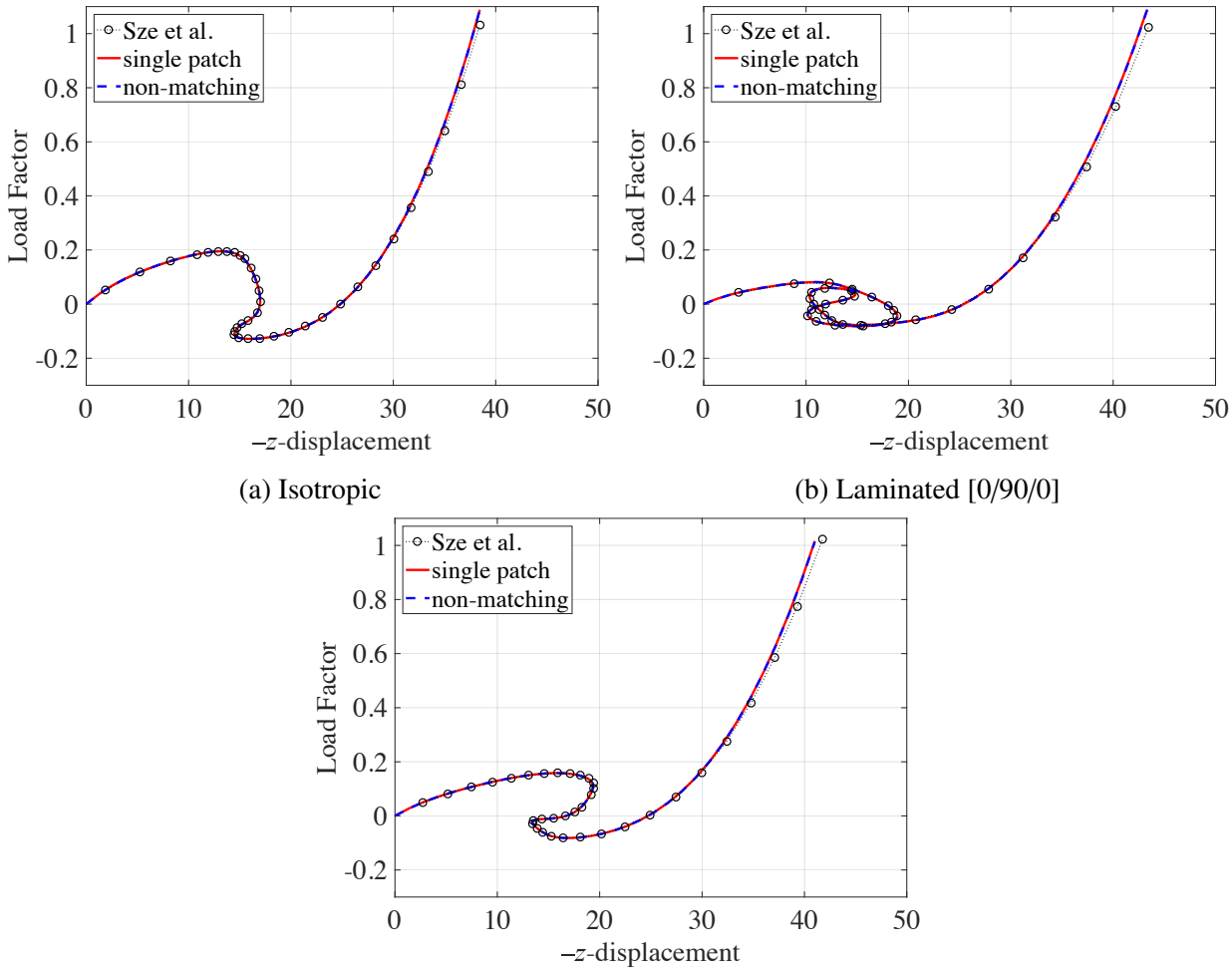

(a) Isotropic

(b) Laminated [0/90/0]

(c) Laminated [90/0/90]

Figure 31: Vertical displacement of the central point versus applied distributed load for the nonlinear shallow roof with $\alpha = 10^3$.

multiple non-matching NURBS patches that are coupled using the proposed penalty approach.

4.1. Blade definition

Resor [38] developed a detailed, composite wind turbine blade design based on the basic 5 MW blade design proposed by Jonkman et al. [39]. Resor [38] discusses geometry and material design details as well as comprehensive design analysis procedures. Due to its realistic material distribution, this NREL/SNL 5 MW blade design is a good candidate for demonstrating the effectiveness of the presented coupling methodology for complex composite structures.

Figure 32 shows the NREL/SNL 5 MW wind turbine blade geometry modeled using NURBS surfaces of degree 3. Note that the thick black lines indicate the edges of the 27 NURBS patches. The blade shell is modeled with multiple patches to accurately capture sharp discontinuities in material definition at the patch edges. The shear webs must also be modeled as independent NURBS

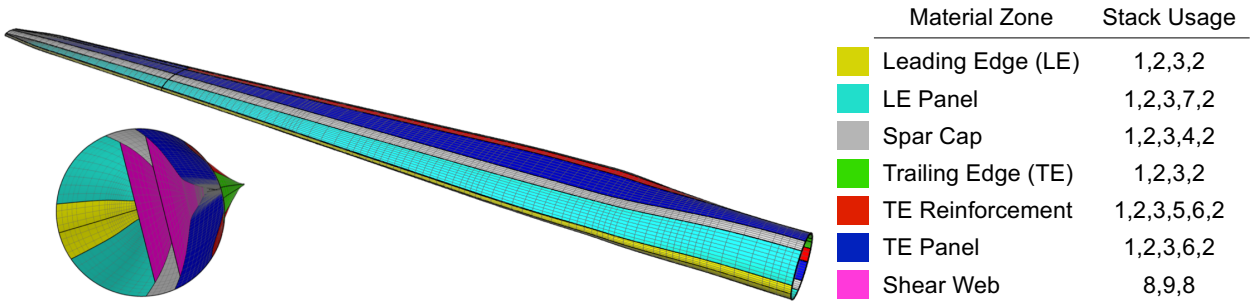

Figure 32: NREL/SNL 5 MW wind turbine blade geometry, discretization, and stack usage for each material zone. Element edges indicated by gray lines, patch edges indicated by thick black lines.

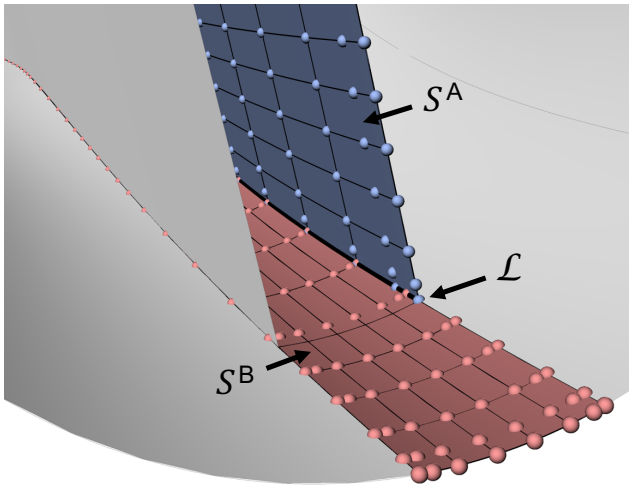

Figure 33: Non-matching discretization between the patches used to model the spar cap (red) and shear web (blue) of a wind turbine blade. Control point locations indicated by spheres.

surfaces. Even in this relatively straightforward geometrical configuration, it is somewhat difficult to ensure matching spanwise discretization for all patches, as shown in Figure 33, highlighting the value of a methodology for coupling non-matching patches.

Each of the colored regions in Figure 32 indicates a unique composite material stacking sequence. Furthermore, each material stack in each of these zones has a unique thickness profile along the blade's span. The stacking sequence in each material zone, in terms of stack ID, is shown in Figure 32. The name, material, and spanwise thickness distribution of each stack is given in Figure 34. Material properties and other details can be seen in Resor [38]. Note that Resor [38] assumes that material thicknesses are constant in between a predefined set of spanwise stations. In the present work, material thicknesses are defined as piecewise linear functions of blade span which are evaluated at every quadrature point when determining homogenized material properties. This smoother material distribution is expected to influence results only slightly.

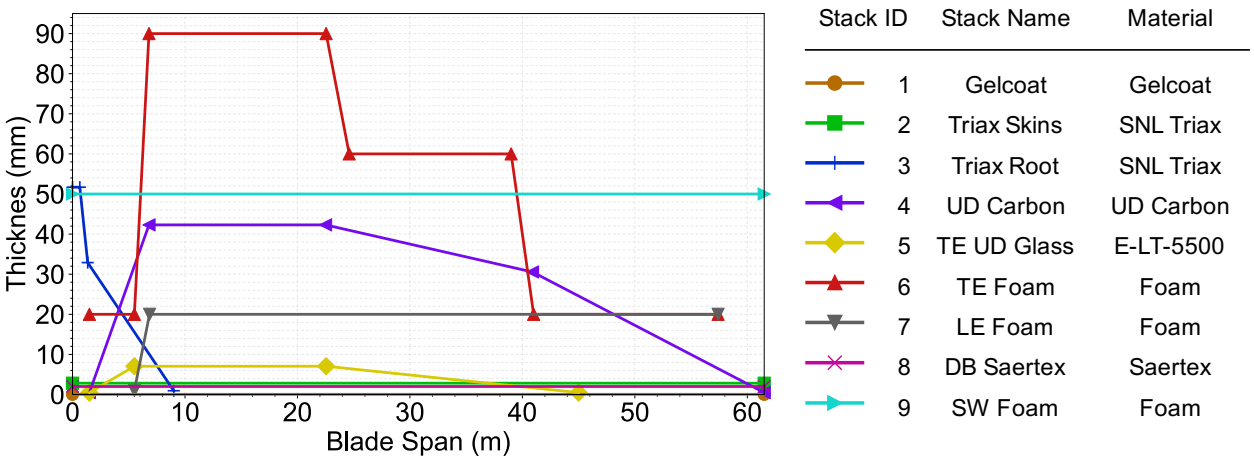

Figure 34: Thickness distribution as a function of blade span for all material stacks as well as stack IDs, names, and materials.

4.2. Linear buckling analysis

All examples considered thus far have been either isotropic configurations, for which the penalty formulations are given by Eqs. (29) and (30), or composite configurations featuring a uniform composite definition, for which the penalty formulations are given by Eqs. (27) and (28). Some composite structures, however, especially wind turbine blades, may have composite definitions that are not uniform. Specifically, sharp material discontinuities can even occur in between, for example, a blade's spar cap—which has a stiff material definition—and the leading and trailing edge panels, which are comparatively weak. Because the penalty parameter formulations should be based on local material properties, it is necessary to identify formulations capable of addressing such discontinuities.

A number of possible formulations which resolve discontinuities in material description are explored here. Linear buckling analysis, as described in Eq. (32), is employed for this study because it is among the most important types of analyses performed for wind turbine blade structural design and because it is one of the primary uses for three-dimensional shell models. Aerodynamic loads are generated using NREL's FAST [40], an aeroelastic wind turbine modeling software that uses engineering models such as blade element momentum theory to simulate the dynamic structural and aerodynamic performance of wind turbines. The NREL/SNL 5 MW wind turbine is simulated under a 50-year extreme wind condition having 70 m/s winds, a fixed rotor, blades feathered to 90°, and 15° of yaw misalignment as specified by design load case (DLC) 6.1 in the IEC 61400 design standard [41]. This is commonly a design-governing load case in wind turbine blade design. The aerodynamic loads at the time instance featuring the largest blade root bending moment in the flapwise direction are collected and applied to the IGA-based buckling analysis through chordwise-constant but spanwise-variable distributed loads.

The various approaches considered for the penalty parameter formulations are described below. In the following, i and j are restricted to $i = 1, 2$ and $j = 1, 2$.

- **Minimum**: The minimum local stiffness between patches A and B is selected. The intent of this method is to yield a penalty value that is sufficiently high locally without producing penalty values that are excessively high with respect to less stiff portions of the model.

$$\alpha_{\mathrm{d}} = \alpha \frac{\min\left(\max_{i,j}\left(\mathbb{A}^{\mathrm{A}}_{ij}\right), \max_{i,j}\left(\mathbb{A}^{\mathrm{B}}_{ij}\right)\right)}{h}, \tag{33}$$

$$\alpha_{\mathrm{r}} = \alpha \frac{\min\left(\max_{i,j}\left(\mathbb{D}^{\mathrm{A}}_{ij}\right), \max_{i,j}\left(\mathbb{D}^{\mathrm{B}}_{ij}\right)\right)}{h}. \tag{34}$$

- **Maximum**: In this method, the maximum local stiffness between patches A and B is selected. This method prioritizes maximizing the influence of the penalty locally.

$$\alpha_{\mathrm{d}} = \alpha \frac{\max\left(\max_{i,j}\left(\mathbb{A}^{\mathrm{A}}_{ij}\right), \max_{i,j}\left(\mathbb{A}^{\mathrm{B}}_{ij}\right)\right)}{h}, \tag{35}$$

$$\alpha_{\mathrm{r}} = \alpha \frac{\max\left(\max_{i,j}\left(\mathbb{D}^{\mathrm{A}}_{ij}\right), \max_{i,j}\left(\mathbb{D}^{\mathrm{B}}_{ij}\right)\right)}{h}. \tag{36}$$

- **Average**: This method dictates that, between patches A and B, the average local stiffness should be used in the penalty formulation. This approach seeks to allow the material properties of both patches to influence the penalty parameter.

$$\alpha_{\mathrm{d}} = \alpha \frac{\max_{i,j}\left(\mathbb{A}^{\mathrm{A}}_{ij}\right) + \max_{i,j}\left(\mathbb{A}^{\mathrm{B}}_{ij}\right)}{2h}, \tag{37}$$

$$\alpha_{\mathrm{r}} = \alpha \frac{\max_{i,j}\left(\mathbb{D}^{\mathrm{A}}_{ij}\right) + \max_{i,j}\left(\mathbb{D}^{\mathrm{B}}_{ij}\right)}{2h}. \tag{38}$$

- **Minimum Transverse**: In this approach, the material matrices are rotated such that the $\mathring{\mathbf{e}}_1$ direction of the rotated matrices, $\tilde{\mathbb{A}}$ and $\tilde{\mathbb{D}}$, is consistent with the local tangential direction of the penalty curve. Then, the stiffness transverse to the penalty curve, or $\tilde{\mathbb{A}}_{22}$ and $\tilde{\mathbb{D}}_{22}$, can be directly used in the formulation. Between the two patches, the minimum $\tilde{\mathbb{A}}_{22}$ or $\tilde{\mathbb{D}}_{22}$ is selected, citing the same logic employed in the "Minimum" approach.

$$\alpha_{\mathrm{d}} = \alpha \frac{\min\left(\tilde{\mathbb{A}}^{\mathrm{A}}_{22}, \tilde{\mathbb{A}}^{\mathrm{B}}_{22}\right)}{h}, \tag{39}$$

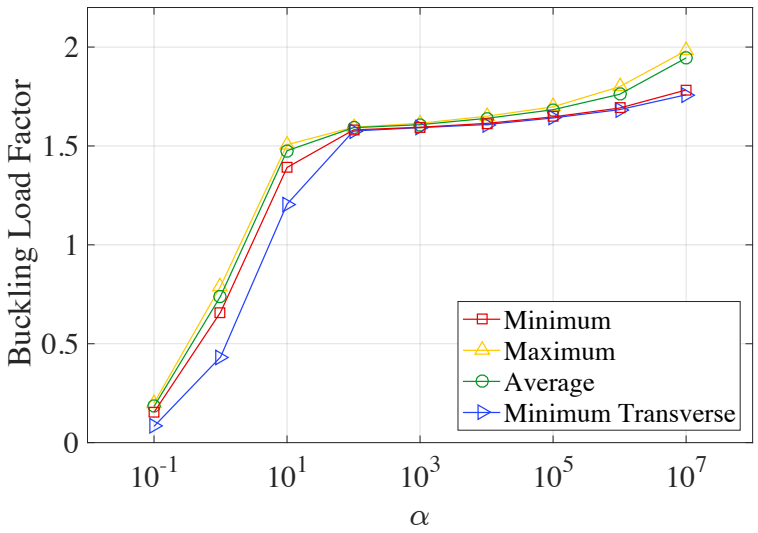

Figure 35: Lowest buckling load factor as a function of α for the various possible methods of formulating the penalty parameter for composite configurations featuring material discontinuities.

$$\alpha_{\mathrm{r}} = \alpha \frac{\min\left(\tilde{\mathbb{D}}^{\mathrm{A}}_{22}, \tilde{\mathbb{D}}^{\mathrm{B}}_{22}\right)}{h} \,. \tag{40}$$

Each of these methods is used with a range of α values in buckling analysis of the NREL/SNL 5 MW blade, as shown in Figure 35. Due to the technical challenges presented in this problem, such as the large number of penalty coupling curves (51) and highly non-uniform material definition across the blade structure, one should not expect a level of α parameter flexibility comparable to that seen in previous benchmark examples. Still, all methods feature a plateau at around $\alpha = 10^2$ to $\alpha = 10^4$, reinforcing the validity of using $\alpha = 10^3$ in general.

Both the "Maximum" and "Average" methods are shown to decrease in accuracy more quickly than the "Minimum" and "Minimum Transverse" methods with increasing α. Because the "Minimum" and "Minimum Transverse" methods utilize similar logic and exhibit comparable performance, we recommend using the "Minimum" method for the sake of implementation simplicity. The first three buckling modes obtained using this approach and $\alpha = 10^3$ are shown in Figure 36, and the "Minimum" method is used for the remainder of the analyses.

4.3. Vibration analysis

A blade's vibration characteristics are another potential design-driver. It is critical that a blade's natural frequencies of vibration do not align with certain turbine operational frequencies, such as the rotor's rotational speed or the fundamental tower frequency, in order to avoid resonance. Linear vibration analysis is performed by considering the eigenvalue problem

$$\left(\mathbf{K}^{\mathrm{lin}} - \lambda_i \mathbf{M}\right) \mathbf{v}_i = 0 \,, \tag{41}$$

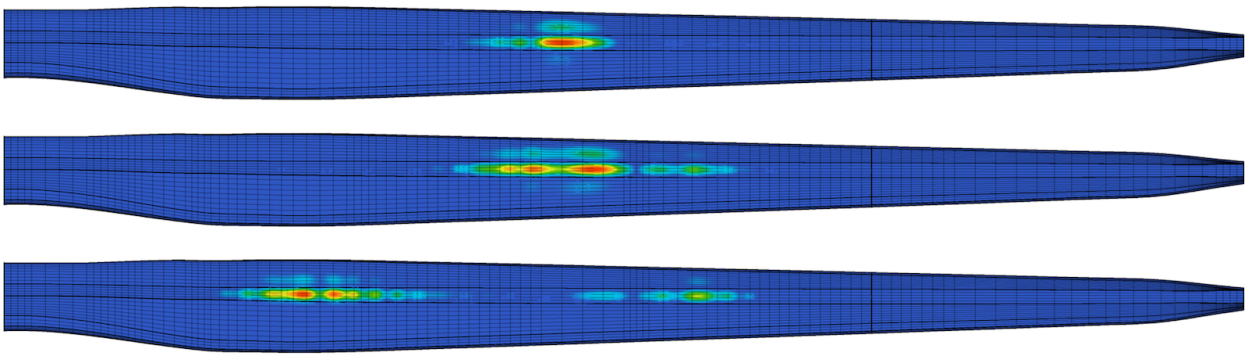

Figure 36: First (top), second (middle), and third (bottom) buckling modes of the NREL/SNL 5 MW blade using $\alpha = 10^3$. Color contour indicates relative magnitude of deflection in buckling.

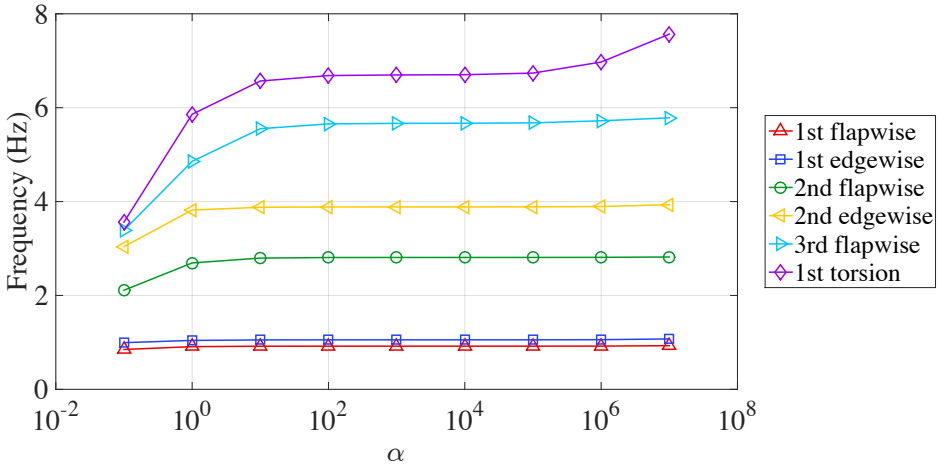

Figure 37: NREL/SNL 5 MW blade frequencies of vibration using the proposed methodology and a range of values of α.

where $\mathbf{K}^{\text{lin}}$ is the linear stiffness matrix of the structure, $\mathbf{M}$ is the mass matrix, and λ_i is the i^{th} eigenvalue associated with mode vector $\mathbf{v}_i$. The relation of the i^{th} frequency of vibration, ω_i, to the eigenvalue is given by the equation $\omega_i^2 = \lambda_i$.

Vibration analysis results using a range of α values are shown in Figure 37. Again, consistent behavior is seen over a range of values of α with $\alpha = 10^3$ remaining appropriate. Because vibration analysis is not load-dependent, the results can also be reasonably compared to the results found in Resor [38]. Although the model developed by Resor [38] does not evaluate the material thickness distributions the same way as the IGA-based framework—that is, material thicknesses aren't evaluated at every quadrature point, leading to a less smooth distribution overall—the comparison in Table 1 demonstrates good agreement overall.

Mode	Ref. Frequency (Hz)	IGA Frequency (Hz)	Difference (%)
1st flapwise	0.87	0.919	5.63
1st edgewise	1.06	1.054	0.57
2nd flapwise	2.68	2.809	4.81
2nd edgewise	3.91	3.886	0.61
3rd flapwise	5.57	5.666	1.72
1st torsion	6.45	6.698	3.84

Table 1: Comparison of vibration analysis results between the reference [38] and the proposed IGA-based method with $\alpha = 10^3$.

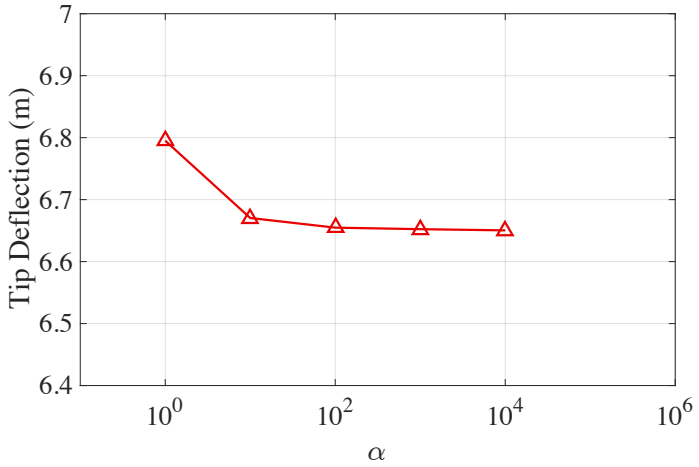

Figure 38: Maximum flapwise tip deflection due to nonlinear analysis for a range of values for α.

4.4. Nonlinear deflection analysis

Maximum blade tip deflection is yet another important consideration in wind turbine blade design, especially as longer and more flexible blades are developed. Care must be taken to ensure that there is appropriate clearance between the rotor and the tower. The same loads that are used in Section 4.2 are applied and nonlinear deformation analysis is performed for a range of α values, as shown in Figure 38.

Because a large number of penalty curves and a variable composite material definition are used, nonlinear convergence is more difficult to achieve for excessively large values of α. Still, a consistent value for tip deflection can be seen from approximately $\alpha = 10^2$ to $\alpha = 10^4$. From $\alpha = 10^2$ to $\alpha = 10^3$, a change in tip deflection of only 0.037% is observed. Similarly, from $\alpha = 10^3$ to $\alpha = 10^4$, a change in tip deflection of 0.029% is observed. This reinforces the validity of using $\alpha = 10^3$ in general and indicates that the proposed method is appropriate for nonlinear analysis of structures featuring material stiffness discontinuities at patch-coupling interfaces. Finally, the nonlinear deformation of the NREL/SNL 5 MW blade using $\alpha = 10^3$ is shown in Figure 39.

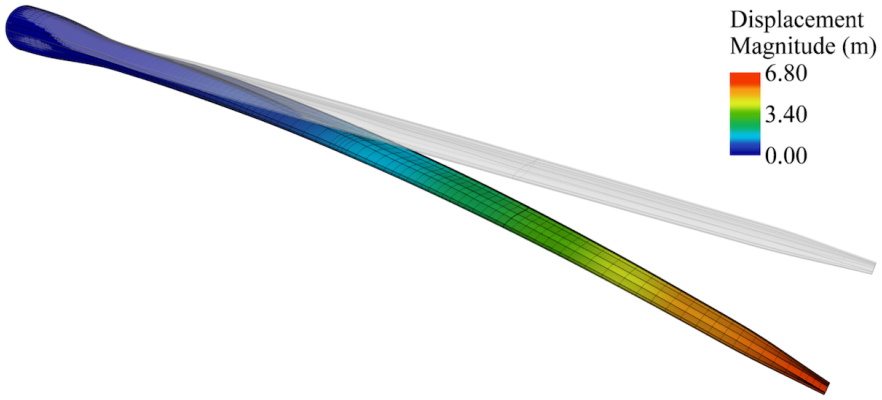

Figure 39: Deformation of the NREL/SNL 5 MW blade due to nonlinear analysis using $\alpha = 10^3$.

5. Conclusion

A new approach for penalty coupling of NURBS patches with non-matching interfaces is proposed. The proposed penalty parameters are dimensionally consistent and the choice of the penalty coefficient is problem-independent. The formulations are based on local stiffness properties and are stated for isotropic and composite configurations, as well as for the unique case of composite configurations with stiffness discontinuities at the coupling interface.

The proposed patch coupling approach is demonstrated on a number of benchmark problems from the literature. For all problems, accurate kinematic performance is observed for a relatively consistent range of penalty coefficient values. As a result, it is suggested that a dimensionless value of $\alpha = 10^3$ be used regardless of problem type or configuration. Through the benchmark problems, the method is shown to be useful for linear, nonlinear, and buckling analyses, for both matching and non-matching discretizations, and for problems involving both isotropic and composite materials.

In order to demonstrate the utility of the proposed approach for complex, large-scale industrial problems, the penalty coupling methodology is applied to the NREL/SNL 5 MW wind turbine blade, a realistic blade model with spanwise- and chordwise-variant composite material definitions. Patch boundaries are used to capture sharp material discontinuities; the blade is therefore modeled using 27 NURBS patches and 51 penalty coupling curves. Because it has a composite definition with a number of material stiffness discontinuities, this example is used to confirm the good performance of the proposed penalty parameter formulations relative to some alternative formulations. Buckling, vibration, and deformation analyses are performed. Using $\alpha = 10^3$, analysis results that are reasonably consistent with the reference results are obtained. Thus, the proposed patch coupling approach has great potential for addressing a wide variety of multi-patch shell analysis problems.

As previously mentioned, one potentially fruitful future use of this methodology would be to use it in the context of trimmed NURBS geometries. For complex geometries, patch intersections

are commonly used to trim NURBS patches. In the analysis setting, these interfaces are often considered to be rigidly coupled. Hence, the proposed penalty methodology could be applied to such trimming curves, which are defined in the parametric space of the NURBS surfaces. Of course, some other approach, such as adaptive refinement, would have to be employed to accommodate proper treatment of the trimmed portions of the NURBS surfaces.

Finally, although only linear elastic material behavior is considered in this work, we believe the proposed penalty formulations can be readily extended to nonlinear materials. This will also be investigated in the future.

Acknowledgments

A.J. Herrema and E.L. Johnson were supported by the U.S. National Science Foundation (NSF) Grant No. DGE-1069283 which funds the activities of the Integrative Graduate Education and Research Traineeship (IGERT) in Wind Energy Science, Engineering, and Policy (WESEP) at Iowa State University. J. Kiendl was partially supported by the Onsager fellowship program of the Norwegian University of Science and Technology. This support is gratefully acknowledged.

References

[1] Y. Bazilevs, V.M. Calo, J.A. Cottrell, J.A. Evans, T.J.R. Hughes, S. Lipton, M.A. Scott, and T.W. Sederberg. Isogeometric analysis using T-splines. *Computer Methods in Applied Mechanics and Engineering*, 199:229–263, 2010.

[2] T.J.R. Hughes, J.A. Cottrell, and Y. Bazilevs. Isogeometric analysis: CAD, finite elements, NURBS, exact geometry and mesh refinement. *Computer Methods in Applied Mechanics and Engineering*, 194:4135–4195, 2005.

[3] J. Kiendl, K.-U. Bletzinger, J. Linhard, and R. Wüchner. Isogeometric shell analysis with Kirchhoff–Love elements. *Computer Methods in Applied Mechanics and Engineering*, 198: 3902–3914, 2009.

[4] D.J. Benson, Y. Bazilevs, M.-C. Hsu, and T.J.R. Hughes. A large deformation, rotation-free, isogeometric shell. *Computer Methods in Applied Mechanics and Engineering*, 200: 1367–1378, 2011.

[5] N. Nguyen-Thanh, J. Kiendl, H. Nguyen-Xuan, R. Wüchner, K.-U. Bletzinger, Y. Bazilevs, and T. Rabczuk. Rotation free isogeometric thin shell analysis using PHT-splines. *Computer Methods in Applied Mechanics and Engineering*, 200(47-48):3410–3424, 2011.

[6] J. Kiendl, M.-C. Hsu, M.C.H. Wu, and A. Reali. Isogeometric Kirchhoff–Love shell formulations for general hyperelastic materials. *Computer Methods in Applied Mechanics and Engineering*, 291:280–303, 2015.

[7] A. Buganza Tepole, H. Kabaria, K.-U. Bletzinger, and E. Kuhl. Isogeometric Kirchhoff–Love shell formulations for biological membranes. *Computer Methods in Applied Mechanics and Engineering*, 293:328–347, 2015.

[8] M. Bischoff, W.A. Wall, K.-U. Bletzinger, and E. Ramm. Models and finite elements for thin-walled structures. In E. Stein, R. de Borst, and T.J.R. Hughes, editors, *Encyclopedia of Computational Mechanics*, Volume 3: Solids and Structures, chapter 3. John Wiley & Sons, 2004.

[9] J. Kiendl, Y. Bazilevs, M.-C. Hsu, R. Wüchner, and K.-U. Bletzinger. The bending strip method for isogeometric analysis of Kirchhoff–Love shell structures comprised of multiple patches. *Computer Methods in Applied Mechanics and Engineering*, 199:2403–2416, 2010.

[10] A. Goyal and B. Simeon. On penalty-free formulations for multipatch isogeometric kirchhoff–love shells. *Mathematics and Computers in Simulation*, 136:78–103, 2017.

[11] Z. Lei, F. Gillot, and L. Jezequel. A C^0/G^1 multiple patches connection method in isogeometric analysis. *Applied Mathematical Modelling*, 39(15):4405–4420, 2015.

[12] M. Breitenberger, A. Apostolatos, B. Philipp, R. Wüchner, and K.-U. Bletzinger. Analysis in computer aided design: Nonlinear isogeometric B-Rep analysis of shell structures. *Computer Methods in Applied Mechanics and Engineering*, 284:401–457, 2015.

[13] T.X. Duong, F. Roohbakhshan, and R.A. Sauer. A new rotation-free isogeometric thin shell formulation and a corresponding continuity constraint for patch boundaries. *Computer Methods in Applied Mechanics and Engineering*, 316:43–83, 2017.

[14] W. Dornisch, G. Vitucci, and S. Klinkel. The weak substitution method - an application of the mortar method for patch coupling in NURBS-based isogeometric analysis. *International Journal for Numerical Methods in Engineering*, 103(3):205–234, 2015.

[15] E. Brivadis, A. Buffa, B. Wohlmuth, and L. Wunderlich. Isogeometric mortar methods. *Computer Methods in Applied Mechanics and Engineering*, 284:292–319, 2015.

[16] Y. Guo and M. Ruess. Nitsche's method for a coupling of isogeometric thin shells and blended shell structures. *Computer Methods in Applied Mechanics and Engineering*, 284:881–905, 2015.

[17] Y. Guo, J. Heller, T.J.R. Hughes, M. Ruess, and D. Schillinger. Variationally consistent iso-

geometric analysis of trimmed thin shells at finite deformations, based on the STEP exchange format. *Computer Methods in Applied Mechanics and Engineering*, 336:39–79, 2018.

[18] N. Nguyen-Thanh, K. Zhou, X. Zhuang, P. Areias, H. Nguyen-Xuan, Y. Bazilevs, and T. Rabczuk. Isogeometric analysis of large-deformation thin shells using RHT-splines for multiple-patch coupling. *Computer Methods in Applied Mechanics and Engineering*, 316: 1157–1178, 2017.

[19] L. Coox, F. Greco, O. Atak, D. Vandepitte, and W. Desmet. A robust patch coupling method for NURBS-based isogeometric analysis of non-conforming multipatch surfaces. *Computer Methods in Applied Mechanics and Engineering*, 316:235–260, 2017.

[20] Y. Bazilevs, M.-C. Hsu, J. Kiendl, R. Wüchner, and K.-U. Bletzinger. 3D simulation of wind turbine rotors at full scale. Part II: Fluid–structure interaction modeling with composite blades. *International Journal for Numerical Methods in Fluids*, 65:236–253, 2011.

[21] J.N. Reddy. *Mechanics of Laminated Composite Plates and Shells: Theory and Analysis, 2nd ed.* CRC Press, Boca Raton, FL, 2004.

[22] J. Kiendl. *Isogeometric Analysis and Shape Optimal Design of Shell Structures*. PhD thesis, Lehrstuhl für Statik, Technische Universität München, 2011.

[23] Y. Bazilevs, M.-C. Hsu, and M.A. Scott. Isogeometric fluid–structure interaction analysis with emphasis on non-matching discretizations, and with application to wind turbines. *Computer Methods in Applied Mechanics and Engineering*, 249–252:28–41, 2012.

[24] V. Hernandez, J.E. Roman, and V. Vidal. SLEPc: A scalable and flexible toolkit for the solution of eigenvalue problems. *ACM Trans. Math. Software*, 31(3):351–362, 2005.

[25] J.E. Roman, C. Campos, E. Romero, and A. Tomas. SLEPc users manual. Technical Report DSIC-II/24/02 - Revision 3.7, D. Sistemes Informàtics i Computació, Universitat Politècnica de València, Valencia, Spain, 2016.

[26] M.A. Crisfield. A fast incremental/iterative solution procedure that handles "snap-through". *Computers & Structures*, 13(1–3):55–62, 1981.

[27] T. Belytschko, H. Stolarski, W.K. Liu, N. Carpenter, and J.S.-J. Ong. Stress projection for membrane and shear locking in shell finite elements. *Computer Methods in Applied Mechanics and Engineering*, 51:221–258, 1985.

[28] S. Timoshenko and S. Woinowsky-Krieger. *Theory of Plates and Shells (Engineering Societies Monograph), 2nd ed.* McGraw-Hill, 1959.

[29] K.Y. Sze, X.H. Liu, and S.H. Lo. Popular benchmark problems for geometric nonlinear

analysis of shells. *Finite Elements in Analysis and Design*, 40:1551–1569, 2004.

[30] M. Smith. *ABAQUS/Standard User's Manual, Version 6.9*. Simulia, 2009.

[31] A. Korobenko, M.-C. Hsu, I. Akkerman, J. Tippmann, and Y. Bazilevs. Structural mechanics modeling and FSI simulation of wind turbines. *Mathematical Models and Methods in Applied Sciences*, 23(2):249–272, 2013.

[32] Y. Bazilevs, A. Korobenko, X. Deng, and J. Yan. Novel structural modeling and mesh moving techniques for advanced fluid-structure interaction simulation of wind turbines. *International Journal for Numerical Methods in Engineering*, 102(3-4):766–783, 2014.

[33] M.-C. Hsu and Y. Bazilevs. Fluid–structure interaction modeling of wind turbines: simulating the full machine. *Computational Mechanics*, 50:821–833, 2012.

[34] J. Yan, A. Korobenko, X. Deng, and Y. Bazilevs. Computational free-surface fluid–structure interaction with application to floating offshore wind turbines. *Computers & Fluids*, 141: 155–174, 2016.

[35] Y. Bazilevs, A. Korobenko, X. Deng, and J. Yan. Fluid–structure interaction modeling for fatigue-damage prediction in full-scale wind turbine blades. *Journal of Applied Mechanics*, 83:061010–061010–9, 2016.

[36] M.-C. Hsu, C. Wang, A.J. Herrema, D. Schillinger, A. Ghoshal, and Y. Bazilevs. An interactive geometry modeling and parametric design platform for isogeometric analysis. *Computers and Mathematics with Applications*, 70:1481–1500, 2015.

[37] A.J. Herrema, N.M. Wiese, C.N. Darling, B. Ganapathysubramanian, A. Krishnamurthy, and M.-C. Hsu. A framework for parametric design optimization using isogeometric analysis. *Computer Methods in Applied Mechanics and Engineering*, 316:944–965, 2016.

[38] B.R. Resor. Definition of a 5MW/61.5m wind turbine blade reference model. Technical Report SAND2013-2569, Sandia National Laboratories, Albuquerque, NM, 2013.

[39] J. Jonkman, S. Butterfield, W. Musial, and G. Scott. Definition of a 5-MW reference wind turbine for offshore system development. Technical Report NREL/TP-500-38060, National Renewable Energy Laboratory, Golden, CO, 2009.

[40] J.M. Jonkman and M.L. Buhl Jr. FAST user's guide. Technical Report NREL/EL-500-38230, National Renewable Energy Laboratory, Golden, CO, 2005.

[41] Wind turbines–Part 1: Design requirements. Technical Report IEC 61400-1, International Electrotechnical Commission, Geneva, Switzerland, 2005.